

AD-A182 355

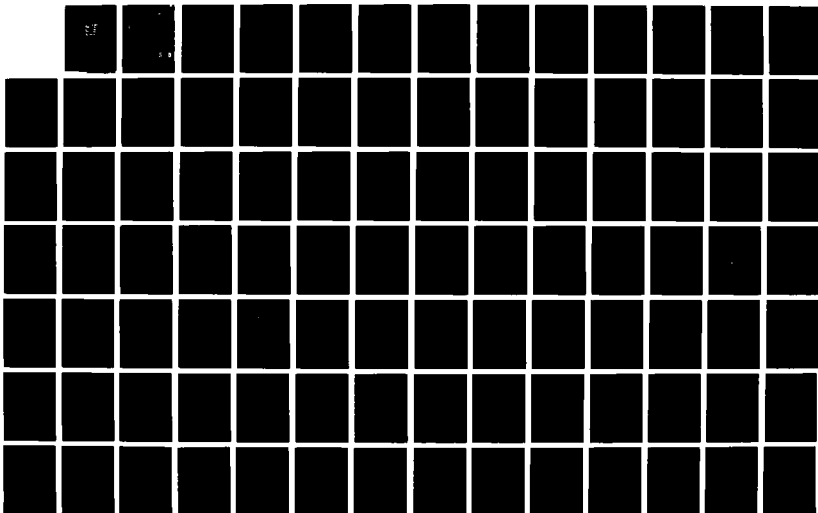
STATIC PRESSURE DISTRIBUTION ON LONG CYLINDERS AS  
FUNCTION OF ANGLE OF YAW (U) MICHIGAN UNIV ANN ARBOR  
DEPT OF AEROSPACE ENGINEERING T WEI ET AL. JUL 83  
N00014-76-C-0571

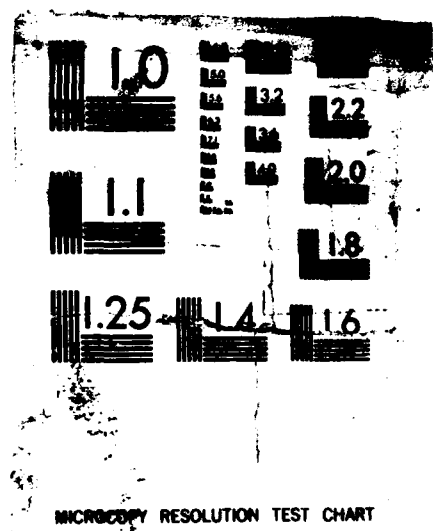
1/2

UNCLASSIFIED

F/G 20/4

NL





9

014439-02

DTIC FILE COPY

STATIC PRESSURE DISTRIBUTION ON LONG CYLINDERS AS  
FUNCTION OF ANGLE OF YAW AND REYNOLDS NUMBER

Timothy Wei and W. W. Willmarth

Sponsored by Department of the Navy  
Office of Naval Research  
Contract N00014-76-C-0571

AD-A182 355

Department of Aerospace Engineering  
University of Michigan, Ann Arbor, Michigan 48109

July 1983

DTIC  
ELECTE  
JUL 15 1987  
S D  
E

UNCLASSIFIED DISTRIBUTION UNLIMITED

# ABSTRACT

Mean pressure measurements around three yawed circular cylinders (aspect ratios of 28, 64, and 100) were made to determine the effect of changes in yaw angle and freestream velocity on the average pressure coefficient,  $C_{PN}$  and the drag coefficient,  $C_{DN}$ . The existence of four distinct types of circumferential pressure distributions, subcritical, transitional, supercritical, and asymmetric, were confirmed along with the appropriateness of scaling  $\bar{C}_{PN}$  and  $C_{DN}$  on a streamwise Reynolds number,  $Re_{sw}$ , based on the freestream velocity and the fluid path length along the cylinder in the streamwise direction. It was found that there is a distinct difference in the values of  $C_{DN}$  and  $\bar{C}_{PN}$  at identical  $Re_{sw}$  for cylinders yawed between  $5^\circ$  and  $60^\circ$ , and for cylinders at greater than  $60^\circ$  yaw. Below  $5^\circ$  of yaw, there are no large scale vortices in the near wake, and  $C_{DN}$  and  $\bar{C}_{PN}$  appear to become independent of  $Re_{sw}$ . At a given yaw angle, between  $5^\circ$  and  $60^\circ$ ,  $\bar{C}_{PN}$  may vary by as much as  $\pm 50\%$  of some mean value.

# TABLE OF CONTENTS

	Page
ABSTRACT . . . . .	iii
LIST OF FIGURES . . . . .	vii
NOMENCLATURE . . . . .	xiii
1. INTRODUCTION . . . . .	1
2. APPARATUS . . . . .	6
2.1 Wind Tunnel and Model	
2.2 Pressure Measuring Apparatus	
3. EXPERIMENTAL METHOD . . . . .	14
3.1 Transducer Calibration	
3.2 Pressure Measurement Procedure	
3.3 Data Processing	
4. RESULTS AND DISCUSSION . . . . .	18
4.1 Introduction	
4.2 Classification of the Results for $\gamma = 5$ to 30 Degrees	
4.3 Asymmetric $C_{pN}$ Profile	
4.4 Discussion of 5-30 Degree Results	
4.5 Small Yaw Angle Results	
5. CONCLUSIONS . . . . .	38
REFERENCES . . . . .	39
FIGURES . . . . .	41



Accession For	
NTIS GRA&I	<input checked="" type="checkbox"/>
DTIC TAB	<input type="checkbox"/>
Unannounced	<input type="checkbox"/>
Justification	
By _____	
Distribution/	
Availability Codes	
Dist	Avail and/or Special
A-1	

## LIST OF FIGURES

- Figure 1. Schematic diagram illustrating the component parts, assembly, and mounting of a cylinder.
- Figure 2. Schematic diagram showing the relative location and connection of the pressure sensing equipment.
- Figure 3. Schematic top-view diagram showing the mounted cylinder and the various flow parameters.
- Figure 4. Combined plot of  $\bar{C}_p$  versus  $\gamma$  for all of the cases tested. The open symbols represent the  $L/D = 28$  data, solid points represent the  $L/D = 64$  data, and the two tone points represent the  $L/D = 100$  data. The symbols  $\circ$ ,  $\square$ ,  $\diamond$ ,  $\triangle$ , and  $\nabla$  correspond to velocities  $U_\infty = 61, 113, 147, 179$ , and  $223$  ft/sec respectively.
- Figure 5. Representative example of a subcritical type of  $C_{pN}$  versus  $\theta$  profile. A potential solution curve is overplotted for comparison. The profile was taken at  $U_\infty = 148$  ft/sec,  $\gamma = 30^\circ$ , and  $L/D = 28$ .
- Figure 6. Plot of  $C_{DN}$  versus  $Re_{sw}$  for the laminar separation data. In all cases,  $L/D = 28$  with  $U_\infty$  varying from 60 to 180 ft/sec. The plot symbols  $\diamond$ ,  $\triangle$ ,  $\nabla$ , and  $\triangleleft$  represent yaw angles of  $15^\circ$ ,  $20^\circ$ ,  $25^\circ$ , and  $30^\circ$  respectively.
- Figure 7. Plot of  $\bar{C}_{pN}$  versus  $Re_{sw}$  for the same subcritical data plotted in Figure 6.

- Figure 8. Isolated plot of  $\bar{C}_p$  versus  $\gamma$  for the subcritical data shown in Figures 6 and 7. The symbols  $\bigcirc$ ,  $\square$ ,  $\diamond$ , and  $\triangle$  represent velocities,  $U_\infty = 61, 113, 147, \text{ and } 179$  ft/sec.
- Figure 9. Representative example of a transitional type of  $C_{pN}$  versus  $\theta$  profile overplotted by a potential solution profile. This profile was taken at  $U_\infty = 179$  ft/sec,  $\gamma = 15^\circ$ , and  $L/D = 64$ .
- Figure 10. Plot of  $C_{DN}$  versus  $Re_{sw}$  for the transitional data. The solid points represent the  $L/D = 64$  data and the open points represent the  $L/D = 28$  data. The symbols  $\square$ ,  $\diamond$ , and  $\triangle$  correspond to  $\gamma = 10^\circ, 15^\circ$ , and  $20^\circ$  respectively.
- Figure 11. Plot of  $\bar{C}_{pN}$  versus  $Re_{sw}$  for the same transitional data plotted in Figure 10.
- Figure 12. Isolated plot of  $C_p$  versus  $\gamma$  for the transitional data shown in Figures 10 and 11. The symbols  $\square$ ,  $\diamond$ , and  $\triangle$  correspond to  $U_\infty = 113, 147, \text{ and } 179$  ft/sec. Again, the open points represent the  $L/D = 28$  data and the solid points are for the  $L/D = 64$  data.
- Figure 13. Representative example of a supercritical type of  $C_{pN}$  versus  $\theta$  profile overplotted with a potential solution profile. This profile was taken at  $U_\infty = 223$  ft/sec,  $\gamma = 10^\circ$ , and  $L/D = 28$ .

- Figure 14. Plot of  $C_{DN}$  versus  $Re_{sw}$  for the supercritical data. The solid, open, and two tone points correspond to the L/D ratios of 64, 28, and 100 respectively. The  $\square$  shaped points represent the  $10^\circ$  yaw case, and the  $\diamond$  shaped points correspond to the  $15^\circ$  yaw case.
- Figure 15. Plot of  $\bar{C}_{pN}$  versus  $Re_{sw}$  for the same supercritical data plotted in Figure 14.
- Figure 16. Isolated plot of  $\bar{C}_p$  versus  $\gamma$  for the supercritical data shown in Figures 14 and 15. The symbols  $\square$ ,  $\diamond$ ,  $\Delta$ , and  $\nabla$  represent  $U_\infty = 113, 147, 179, \text{ and } 223$  ft/sec with the open, solid, and two tone points corresponding to L/D ratios of 28, 64, and 100 respectively.
- Figure 17. Representative sketches of the three types of  $C_{pN}$  versus  $\theta$  profiles reported thus far; (a) laminar separation, (b) transitional, and (c) turbulent separation. The quantitative information in these plots is approximate.
- Figure 18. Representative example of an asymmetric type of  $C_{pN}$  versus  $\theta$  profile along with a potential solution profile. The profile was taken for  $U_\infty = 114$  ft/sec,  $\gamma = 17.5^\circ$ , and  $L/D = 64$ .
- Figure 19. Representative example of an asymmetric type of  $C_{pN}$  versus  $\theta$  profile along with a potential solution profile. This profile was taken at  $U_\infty = 61$  ft/sec,  $\gamma = 15^\circ$ , and  $L/D = 64$ .

- Figure 20. Plot of  $C_{DN}$  versus  $Re_{sw}$  for the asymmetric profile data. The open, solid, and two tone points are representative of the L/D ratios, 28, 64, and 100 respectively. The symbols  $\circ$ ,  $\square$ ,  $\diamond$ , and  $\triangleright$  correspond to yaw angles of  $5^\circ$ ,  $10^\circ$ ,  $15^\circ$ , and  $17.5^\circ$  respectively.
- Figure 21. Plot of  $\bar{C}_{pN}$  versus  $Re_{sw}$  for the same asymmetric profile data shown in Figure 20.
- Figure 22. Isolated plot of  $\bar{C}_p$  versus  $\gamma$  for the asymmetric data shown in Figures 20 and 21. The  $\circ$ ,  $\square$ ,  $\Delta$ , and  $\nabla$  shapes correspond to  $U_\infty = 61, 113, 179, \text{ and } 223 \text{ ft/sec}$ . Again, the open, solid, and two tone points represent L/D ratios of 28, 64, and 100 respectively.
- Figure 23. Combined plot of  $C_{DN}$  versus  $Re_{sw}$  comparing the results of the present study with those of Bursnall and Loftin (1951). Open and solid points correspond to L/D ratios of 28 and 64 while Bursnall and Loftin's data appear as two tone circles.
- Figure 24. Linear regression fit lines of the data in Figure 23. The solid line is a fit of Bursnall and Loftin's (1951)  $60^\circ$  and  $75^\circ$  angle data.  $— . —$  represents the L/D = 28 fitted line,  $— .. —$  corresponds to the L/D = 64 fitted line, and the dashed line is a reproduction of the  $90^\circ$  yaw curve plotted in Schlichting (1979).

Figure 25. Linear regression fit lines of the data in Figure 23. The solid line is a fit of Bursnall and Loftin's (1951) 30° and 45° angle data. Again — . — represents the L/D = 28 fitted line, and — .. — represents the L/D = 64 fitted line.

Figure 26. Combined plot of  $\bar{C}_{pN}$  versus  $Re_{sw}$  for the present study. Open, solid, and two tone points correspond to the L/D ratios, 28, 64, and 100 respectively.

Figure 27. Trend lines of the L/D = 28 data (— - —), the L/D = 64 data (———), and Roshko's (1961) base pressure coefficient data (-----).

Figure 28. Example of a  $C_{pN}$  versus  $\theta$  profile which does not fall into any of the four categories already reported. The profile was taken at  $U_\infty = 179$  ft/sec,  $\gamma = 5^\circ$ , and L/D = 64.

Figure 29.  $C_{DN}$  versus  $Re_{sw}$  plot for the small yaw angle data which did not fall into the subcritical, transitional, supercritical, or asymmetric categories. The symbols  $\bigcirc$ ,  $\square$ ,  $\diamond$ , and  $\triangle$  represent yaw angles of 1°, 2°, 2.5°, and 5° respectively. The open, solid, and two tone points correspond to the L/D ratios of 28, 64, and 100.

Figure 30.  $\bar{C}_{pN}$  versus  $Re_{sw}$  plot for the same small angle data shown in Figure 29.

## NOMENCLATURE

D	cylinder diameter
L	distance from the nose to the measuring station
$\theta$	azimuthal angle measured counter-clockwise from the cylinder forward "stagnation" line
$U_\infty$	free-stream velocity
	yaw angle between free-stream direction and cylinder axis
$U_N = U_\infty \sin \gamma$	component of the free-stream velocity perpendicular to the cylinder
$\nu$	kinematic viscosity
$Re = U_\infty D/\nu$	Reynolds number based on free-stream velocity and diameter for a perpendicularly aligned cylinder
$Re_{sw} = U_\infty (D/\sin \gamma)/\nu$	Reynolds number based on free-stream velocity and streamwise length
$C_{D90^\circ} = \text{drag}/(1/2 \rho U_\infty^2 D)$	drag coefficient based on the drag force perpendicular to the cylinder and free-stream velocity for a perpendicularly aligned cylinder
$C_{DN} = \text{drag}/(1/2 \rho U_N^2 D)$	drag coefficient based on the drag force perpendicular to the cylinder and the normal component of velocity, $U_N$
$C_p = (p - p_\infty)/(1/2 \rho U_\infty^2)$	local pressure coefficient based on free-stream velocity
$C_{pN} = C_p (U_\infty/U_N)^2$	local pressure coefficient based on the normal component of free-stream velocity

$$\bar{C}_p = (\overline{p - p_\infty}) / (1/2 \rho U_\infty^2)$$

average pressure coefficient  
around the cylinder

$$\bar{C}_{pN} = \bar{C}_p (U_\infty / U_N)^2$$

average pressure coefficient  
around the cylinder based on  $U_N$

$$\bar{C}_{pB}$$

average base pressure coefficient  
as defined by Roshko (1960)

$$C_{p90^\circ}$$

average pressure coefficient  
around a perpendicularly  
aligned cylinder

## 1. INTRODUCTION

The problem addressed in this investigation is that of the static pressure distribution developed on the surface of a long circular cylinder immersed in a laminar flow at small angles of yaw. The interest in this problem lies in the direct applicability to the measurement of local static pressures using a static pressure probe. Because the cylinder disturbs the flow, even for the zero yaw angle case, it is necessary to understand the relationship between the measured pressure at the cylinder surface and the actual static pressure of the flow. It is well known that the flow over a circular cylinder, which has its axis aligned perpendicular to the flow, is not at all simple. However, the flow over a yawed cylinder is further complicated by the non-symmetry of the geometry.

Willmarth et al. (1977) showed that the axial symmetry of the boundary layer formed on a cylinder is highly sensitive to small yaw angles which, in turn, might affect the average pressure readings reported by the pressure probe. Thus, unless the attitude of the probe, relative to the flow direction, is known at all times, the static pressure developed on the surface of the probe may not be characteristic of the static pressure in the flow. It was the intent of this investigation to determine the effect of changes in yaw angle and freestream velocity on the average pressure coefficient around the circumference of a circular cylinder.

The problem of flow over yawed cylinders or cylinders at angle of attack first attracted attention in the 1950's. At that

time, research was carried out to determine the lift and drag characteristics of an aircraft fuselage in supersonic flight.

In the past three decades, a number of significant works were published dealing with yawed cylinder flow at relatively large yaw angles. Bursnall and Loftin (1951) performed exhaustive studies of pressure distributions around cylinders in air. They investigated a yaw angle range of 30 to 90 degrees, over a Reynolds number range, based on cylinder diameter and the component of velocity normal to the cylinder axis, of  $6 \times 10^4$  to  $6 \times 10^5$ . With the distributions obtained, Bursnall and Loftin (1951) identified three types of local pressure profile ( $C_p$  versus  $\theta$ ) shapes and related them to similar profiles obtained around a 90 degree (perpendicular) yawed cylinder. Each shape of profile was characteristic of a different type of cylinder boundary layer separation, i.e. laminar boundary layer separation, laminar separation with turbulent reattachment, and purely turbulent boundary layer separation.

Bursnall and Loftin (1951) used their data to calculate normal drag coefficients and plotted these results against the normal Reynolds number defined in the preceding paragraph. However, much later, Lamont and Hunt (1975) showed that the characteristic length of the cylinder should be  $D/\sin \gamma$ , where  $D$  is the cylinder diameter, and  $\gamma$  is the yaw angle. Thus, defining a stream-wise Reynolds number:

$$Re_{sw} = U_{\infty} D / (v \sin \gamma)$$

Lamont and Hunt (1975) showed that the normal drag coefficients

could be collapsed onto a single  $C_{DN}$  versus  $Re_{sw}$  curve. This result suggests that inviscid sweepback theory may be applicable to yawed cylinder flows.

Inviscid sweepback theory is based on the idea that only the flow normal to the axis of a yawed cylinder affects the lift and drag forces on the cylinder. The flow parallel to the axis of the cylinder contributes identical pressures around the cylinder circumference, assuming axially symmetric flow. Thus, when integrating the pressures around the cylinder to calculate the lift or drag, the axial flow pressure contributions will cancel, leaving only the normal flow contributions. As long as this theory is valid, drag and pressure coefficients can be defined by:

$$\begin{aligned} C_{DN} &= (\text{drag/area}) / (1/2 \rho U_N^2) \\ &= (\text{drag/area}) / (1/2 \rho U_\infty^2 \sin^2 \gamma) \end{aligned}$$

and

$$\begin{aligned} C_{pN} &= (p - p_\infty) / (1/2 \rho U_N^2) \\ &= (p - p_\infty) / (1/2 \rho U_\infty^2 \sin^2 \gamma) \end{aligned}$$

respectively. Measurements of either of these coefficients should collapse onto a single curve, when plotted against  $Re_{sw}$ , and should be identical to that obtained from a perpendicularly aligned cylinder.

For small yaw angles,  $Re_{sw}$  can be very large because of the  $1/\sin \gamma$  in the  $Re_{sw}$  definition. Therefore it was necessary to locate some high Reynolds number data in the literature with which the present data could be compared. Roshko (1961) obtained drag coefficient and base pressure coefficient curves in

pressurized air up to Reynolds numbers  $10^7$  for a perpendicularly aligned cylinder. The  $C_{DN}$  results were independently confirmed by Achenbach (1968) up to Reynolds number of  $5 \times 10^6$ .

The first description of the yawed cylinder wake flow field, put forward by Allen and Perkins (1951), used the flow over an impulsively started cylinder as a model. The idea is that the flow field at a particular position along the length of the yawed cylinder will have a one-to-one correspondence with the flow field at some instant of time in the impulsive flow case. Thomson and Morrison (1971) measured the vorticity in the wake of yawed cylinders in supersonic flows as an extension of their subsonic work and found, for both subsonic and supersonic flows, the strength of the vortices shed from the yawed cylinder do not match the theoretical vortex strengths of the impulse flow model. Referring back to their 1965 work, Thomson and Morrison (1971) concluded that the impulse flow analogy is incorrect, and reiterated their suggestion of a combined Karman vortex street and impulse flow theory to quantitatively correctly describe the yawed cylinder wake.

Clearly, there are many "loose ends" in the study of yawed cylinder flow. It was the intent of this investigation to gain insight which would further the understanding of this difficult problem. Specifically, the research objectives of this investigation were:

- ° to test if inviscid sweepback theory, combined with the  $C_p$  versus  $Re$  and  $C_D$  versus  $Re$  curves from a perpendicularly aligned cylinder, is sufficient to predict  $C_{pN}$  and  $C_{DN}$  at various values of  $Re_{sw}$  for a wide range of yaw angles.
- ° to determine a lower limit where the sweepback formulae are no longer valid, i.e. to extend the current limit of  $\gamma = 30$  degrees down to an, as yet, undetermined lower limit.

## 2. APPARATUS

### 2.1 Wind Tunnel and Model

Mean pressure measurements were made separately on three yawed circular cylinders, 82, 118, and 154 in. in length, in The University of Michigan 5 ft x 7 ft closed circuit wind tunnel. The maximum wind speed in the tunnel was approximately 250 ft/sec with the centerline turbulence level not exceeding 0.6%. Each cylinder was 1.0 in. in diameter and was assembled from two lengths of aluminum tubing, a cylindrical pressure tap segment, and an elliptical nose piece. The 82, 118, and 154 in. cylinders will heretofore be referred to as the short nose, medium nose, and long nose cylinders, respectively.

The cylindrical pressure tap segment, henceforth referred to as the measuring station, was machined from a 5.0 in. length of 1.0 in. outer diameter brass tubing. Twenty four 1/64 in. diameter pressure taps were drilled radially into the brass tube at 15 degree intervals a fixed distance from the end of the tube. Each tap was connected to a short length of 1/16 in. diameter stainless steel tubing to which clear plastic tubing, leading to a transducer and manometer bank, could be connected. Both ends of the measuring station were machined to fit snugly inside the aluminum tubing.

The aluminum tubing was cut from commercially available stock with outer diameter of 1.0 in. and a wall thickness of approximately 1/16 in. Four different lengths of tubing, measuring 23.75 in., 59.75 in., 95.75 in., and 54 in., were cut to form the three cylinders. The 54 in. section of tubing was used as the tail section of all three cylinders. The surfaces of

the four lengths of tubing were sanded to remove extrusion marks and other blemishes, and then were polished with fine steel wool until smooth to the touch.

The nose piece was made from a piece of aluminum rod to form one half of an ellipsoid of revolution with major diameter of 4.5 in. and minor diameter of 1.0 in. An additional cylindrical section extended out from the rear of the nose piece which fit snugly inside the aluminum tubing. To facilitate mounting the longer two cylinders in the wind tunnel, three small holes, approximately 1/64 in. in diameter, were drilled into the nose piece at intervals of 120 degrees. The purpose for these holes will be explained in the following paragraphs. Finally, the nose piece was also sanded and polished with steel wool.

The assembly and mounting of a cylinder in the wind tunnel is schematically illustrated in Figure 1. For all three cylinders, the measuring station, with pressure lines connected, was inserted into the front end of the 54 in. length of aluminum tube. This assembly was rigidly clamped to a T-shaped mounting arm. The arm was in turn bolted to the wind tunnel balance. The pressure lines, extending out the rear of the 54 in. tube, were firmly taped to the tube and the wind tunnel balance, and were brought out of the wind tunnel through a hole in the tunnel floor made for the balance. To the front of the measuring station was placed one of the three remaining lengths of aluminum tubing. Lastly, the elliptical nose was inserted into the front of the cylinder. When assembled, the distance from the nose tip to the pressure taps was 28 in., 64 in., and 100 in. for the short nose,

medium nose, and long nose cylinders respectively. These lengths, when non-dimensionalized with respect to the cylinder diameter,  $L/D = 28, 64, \text{ and } 100$ , will be the characteristic aspect ratios referred to in the remainder of this paper.

For the short nose cylinder,  $L/D = 28$ , the assembly was adequately held together by an internal wire in tension extending through the entire length of the cylinder. Because of the excessive lengths, the internal wire was not sufficient to prevent substantial sag of the two longer cylinders.

To alleviate the sagging problem and to help damp out flow induced vibrations during testing, a guy wire support structure was constructed for use on the medium and long nose cylinders. This is the mounting configuration illustrated in Figure 1. A 3 in. long brass sleeve was cut from 1 1/4 in. outer diameter brass tubing, to which was silver soldered three 1/4 in. square, 12 in. long brass spars. The spars were placed at the leading edge of the sleeve and were evenly spaced 120 degrees apart.

The sleeve was positioned on the cylinder just ahead of the mounting arm and held in place with three set screws. The distance from the pressure taps to the support spars was set at 24 in. to reduce the upstream influence of the spars on the pressure readings. A similar sleeve, to which three eyelets were bolted, was constructed and placed at the extreme rear end of the cylinder. This second sleeve was not pictured in Figure 1 to avoid complicating the schematic.

Music wire, 1/64 in. in diameter, used as the guy wires, was attached to the inside of the elliptical nose piece, passed through one of the three holes drilled in the nose, extended over

one of the support spars, and was firmly tied to a turnbuckle. The turnbuckle was in turn hooked onto one of the eyelets at the end of the cylinder. Three such wires were used to support the cylinders.

When mounted on the wind tunnel balance, the axis of the cylinder was slightly shifted off the tunnel centerline. The cylinder was yawed, using the yaw control of the tunnel balance, until the nose of the cylinder was the same distance from the tunnel centerline as at the mounting point. This position was the zero yaw position. The cylinder was levelled by changing the angle of attack of the balance mount and using a carpenter's level. The cylinder was assumed to be level if the carpenter's level showed that the cylinder was level at the nose, at the mounting point, and at an intermediate location.

For the medium nose cylinder and the long nose cylinder, it was necessary to straighten the cylinder before the angle of attack could be zeroed. This was accomplished by judiciously tightening the guy wires using the turnbuckles placed at the rear of the cylinder. Straightening was done by eye with satisfactory results. However, one problem which could not be corrected was that, even with the guy wires, the cylinder still sagged slightly between the nose and the mounting point. This bend in the cylinder, of the order of one cylinder diameter for the longest cylinder, was expected to affect the results of this investigation. Unfortunately, there was no way to determine the effect of the sag, nor was it possible to ascertain the effect of the guy wires on the flow. The investigation was carried out under the

assumption that the qualitative results would not be affected by these problems, and that the quantitative contamination of the pressure data would be minimal.

## 2.2 Pressure Measuring Apparatus

The apparatus used to measure pressures around the cylinder included the measuring station, a pitot-static tube, a set of glass bottles, a manometer bank, a scani-valve with a pressure transducer, and sundry electronic equipment. The measuring station, described in the previous section, was used to measure the local pressures around the cylinder at 24 equally spaced circumferential intervals. The pitot-static tube was employed to measure the stagnation pressure and the freestream static pressure in the vicinity of the measuring station. This was necessary because the freestream static pressure was not constant along the length of the tunnel test section. The pitot-static probe was suspended through a hole in the tunnel roof and was positioned approximately 18 in. above and upstream of the measuring station.

Time averaging of the pressure signals was done primarily with the aid of a set of 8 oz glass pharmaceutical bottles. There were 26 bottles in all, one for each pressure tap. Since the frequency response of a pressure transducer is inversely proportional to the square root of the volume of fluid in the pressure sensing line [cf Holman (1966)], the use of the 8 oz bottles ensured that the transducer could not detect high frequency pressure fluctuations. A visual check of the system

indicated that the bottled effectively filtered pressure fluctuations higher than approximately 0.2 Hz.

Pressure measurements were made by a Setra Systems Model 237 low range pressure transducer used in conjunction with a 48 channel scani-valve. The scani-valve controller, designed and built at The University of Michigan, had the ability to limit the number of channels the valve scanned (only 26 channels were used in this investigation), and to vary the scanning frequency of the scani-valve. For this study, the time period between successive scans was set between 3 and 5 seconds.

Signal processing and recording was accomplished using a Digitec paper tape punch and digital voltmeter, a Dana Model 2860-V4 variable gain amplifier, and an oscilloscope. The signal from the transducer was filtered and amplified by the Dana amplifier to improve the signal-to-noise ratio of the signal going to the paper tape punch. The amplified signal could be monitored on the oscilloscope and was input into the paper tape punch. Further monitoring of the amplified signal was provided by the Digitec digital voltmeter. This voltmeter was often checked to ensure that the electronics did not saturate and distort the data.

To process the data, the punched paper tape files were read into a Data General Nova-840 mini computer. Input/output devices for the computer included a paper tape reader, line printer, video terminal, and an x-y plotter. Fortran computer programs, written to process and plot the results, will be described in the next section.

Finally, a manometer bank containing 25 oil filled manometers was used as a visual check during the experimental phase of this investigation. The specific gravity of the oil was approximately 0.826 at room temperature. Twenty four of the tubes were connected to the pressure lines coming from the measuring station. The additional manometer was connected to the stagnation pressure line coming from the pitot-static probe.

A schematic diagram showing the relative locations of the pressure sensing equipment is shown in Figure 2. First, the pressure lines, coming from either the measuring station or the pitot-static tube, were connected to the glass pharmaceutical bottles. Coming out of each bottle, the pressure lines were split by a T-junction. One line was connected to the manometer bank (except, of course, for the freestream static pressure signal), and the other line was routed to an input channel on the scani-valve. The freestream static pressure line was also attached to the reference pressure input so that the transducer actually measured the difference between the pressure of interest and the freestream static pressure. Thus, 26 pressure differences were measured by the pressure transducer; the local cylinder pressure differences:

$$P_i - P_\infty$$

the stagnation pressure difference:

$$P_o - P_\infty$$

and the freestream pressure subtracted from itself:

$$P_\infty - P_\infty$$

This last pressure measurement was useful in determining the d.c. offset of the transducer signal. Each of the 26 signals was amplified and filtered by the variable gain amplifier before being recorded by the paper tape punch. The oscilloscope, not shown in Figure 2, was placed between the amplifier output and the paper tape punch input.

### 3. EXPERIMENTAL METHOD

#### 3.1 Transducer Calibration

Before taking data, the output response of the transducer was calibrated. This was necessary in order to calculate the freestream velocity and therefore the Reynolds numbers of the flow. Calibration was done by applying the same pressure on 12 of the pressure lines, noting the pressure in inches of 0.826 specific gravity oil on the manometers, and recording the corresponding transducer output voltages. For each applied pressure, the 12 voltage and the 12 pressure readings were averaged and plotted. This procedure showed that the transducer response is linear up to at least 20 in. of oil, well beyond the range of this investigation. The equation of the calibration line was found to be:

$$\text{output voltage} = 0.10 + 0.15 \times (\text{inches oil})$$

for unit gain on the transducer. This equation was checked several times over a period of several weeks to ensure its validity. It was found that the slope did not change in that time period but the intercept varied by as much as  $\pm 0.05$  volts from day to day. For this reason, the  $p_0 - p_\infty$  transducer reading was created to determine the d.c. offset at the same time that the data were being taken.

#### 3.2 Pressure Measurement Procedure

For every combination of yaw angle and freestream velocity, 28 pressure readings were punched onto a paper tape file. The stagnation and static pressure readings ( $p_0 - p_\infty$  and  $p_\infty - p_\infty$ ) were punched twice and the local cylinder pressure readings were

each punched once ( $p_1 - p_\infty$ ). The reason for this multiple punching and the procedure by which the punching took place will be described in the following paragraphs.

Figure 3 is a schematic top view diagram of the mounted cylinder showing the various parameters and conventions. First, for a given nose length,  $L/D$ , the yaw angle,  $\gamma$ , and the free-stream velocity,  $U_\infty$ , were set. For the data presented in this paper, the yaw angle was always set in the direction shown in Figure 3. Depending on the freestream velocity and yaw angle, a period of up to 5 minutes was allowed for any transients to decay. Subsequent to this delay, the wind tunnel temperature, freestream dynamic pressure, and the atmospheric pressure were recorded. The gain on the Dana variable gain amplifier was set so that the stagnation pressure reading would make optimum use of the 10 volt range of the Digitec voltmeter/paper tape punch. At this gain setting, the stagnation and static pressure readings were punched to a paper tape file. The gain setting was recorded along with the other data.

Immediately after the two pressure readings were punched, the gain on the amplifier was reset so that the largest pressure reading on the cylinder determined by checking the manometer, was also as close to 10 volts as possible. The stagnation pressure reading, the static pressure reading, and the 24 local cylinder pressure readings were punched to complete the 28 point paper tape file. Naturally, the second stagnation pressure reading was erroneous because of saturation of the electronics. However, this point was discarded during data processing, as will be

explained in Section 3.3. The above procedure was repeated for every combination of nose length, yaw angle and freestream velocity examined in this study.

### 3.3 Data Processing

Each 28 point paper tape record was read and stored in the memory of the Data General Nova 840 mini-computer. Fortran computer programs were then run to process the raw data; the output from these programs were either printed, or plotted on a Calcomp model 565 x-y plotter. Some of the salient features of the data reduction algorithm will be discussed in this section.

As explained earlier, it was necessary to remove the d.c. offset from the pressure measurements before further processing could take place. This was done by simply subtracting the appropriate static pressure reading from each of the pressure measurements. Specifically, the first static pressure reading was subtracted from itself and from the first stagnation pressure reading, and the second static pressure reading was subtracted from the remaining 26 data points.

The first stagnation pressure reading was next scaled up so that its amplification gain matched the gain of the 24 local cylinder pressures. The second stagnation pressure was erroneous and was not used. Then, noting that the so-called stagnation pressure reading was actually the freestream dynamic pressure,  $p_o - p_\infty$ , 24 local pressure coefficients were formed by dividing the local pressure readings by the first stagnation pressure (i.e. the dynamic pressure) value.

Local drag coefficients were calculated by multiplying the local pressure coefficients by the cosine of the angular location of the corresponding pressure tap,  $\theta$ . Both the local pressure coefficients and the local drag coefficients were numerically integrated to obtain the average pressure coefficient,  $\overline{C_p}$ , and a total drag coefficient based on the freestream velocity and the force normal to the cylinder axis. Since there were 25 integration steps, the first three steps were integrated using Simpson's 3/8 rule; the remaining 22 integrations were performed using the conventional Simpson's integration rule. Thus the integration is accurate to the order of the 5th power of the step size.

Finally, the wind tunnel density and viscosity were approximately determined by linear interpolation of tabulated values. Interpolation was done by the data reduction program subsequent to the input of the wind tunnel temperature. These values of density and viscosity were used in the calculation of Reynolds numbers.

## 4. RESULTS AND DISCUSSION

### 4.1 Introduction

Pressure measurements from all three cylinders,  $L/D = 28$ , 64, and 100, covering a yaw angle range from 0 to 30 degrees were gathered during this investigation over a freestream velocity range of 60 ft/sec to 225 ft/sec. Figure 4 is a composite plot of average pressure coefficient,  $\overline{C_p}$  versus yaw angle,  $\gamma$ , showing the combinations of freestream velocity, nose length, and yaw angle discussed in this section. The salient features of this plot are the strong reduction in  $\overline{C_p}$  with increasing yaw, and the apparent large amount of scatter in  $\overline{C_p}$  at a given  $\gamma$ . By itself, Fig. 4 does not provide much information regarding the dependence of  $\overline{C_p}$  on the parameters investigated. In the remainder of this section, the results of this investigation will be presented and critically evaluated to gain insight into the behavior of  $\overline{C_p}$ .

### 4.2 Classification of the Results for $\gamma = 5$ to 30 Degrees

The normal drag coefficient and the average normal pressure coefficient,  $\overline{C_{pN}}$ , are closely related in that both coefficients are determined by integrating the local pressures around the cylinder. The difference between the two coefficients is that  $C_{DN}$  is essentially filtered by a  $\cos \theta$  function during integration and  $\overline{C_{pN}}$  is not. Since  $C_{DN}$  and  $\overline{C_{pN}}$  are so closely related, a great deal of information about  $\overline{C_{pN}}$  may be obtained by studying the behavior of  $C_{DN}$ .

Bursnall and Loftin (1951) showed that for flow over a yawed cylinder, for yaw angles greater than 30 degrees, the dependence of the normal drag coefficient,  $C_{DN}$ , on a Reynolds number,  $Re_{sw}$ ,

based on freestream velocity and a streamwise length,  $D/\sin \gamma$ , is identical to the relationship between  $C_{D90^\circ}$  and  $Re$  for a cylinder aligned perpendicular to the flow, Schlichting (1979). For the  $90^\circ$  degree yaw case, the  $C_{D90^\circ}$  dependence on  $Re$  is well known. This dependence has commonly been divided in the literature [cf Roshko (1960)] into three Reynolds number ranges, according to the manner in which the cylinder boundary layer separates from the cylinder. The first range, hereafter referred to as subcritical range, occurs when the cylinder boundary layer remains laminar and separates on the windward side of the cylinder. The second range, the transitional range, is characterized by a laminar separation bubble on the windward side of the cylinder followed by the reattachment of a turbulent boundary layer. The final range, the supercritical range, corresponds to the case where the cylinder boundary layer is turbulent throughout and separates on the leeward side of the cylinder. The type of boundary layer separation can be determined from the pressure distribution,  $C_{pN}$  versus  $\theta$ , plot as will be demonstrated in the following paragraphs.

An example of a laminar separation (subcritical range)  $C_{pN}$  versus  $\theta$  profile is illustrated in Fig. 5. The plot was generated from data gathered while the cylinder was yawed at  $30^\circ$  degrees in a 148 ft/sec flow. A  $C_p$  versus  $\theta$  plot derived from potential flow theory is included for comparison. The salient features of the subcritical range profile are the sharp pressure peaks at  $\theta \approx 70^\circ$  and  $290^\circ$  degrees, indicating separation, followed by a flat base pressure.

Subcritical pressure profiles are found in the low to medium Reynolds number range,  $\sim 300 < Re < 2 \times 10^5$ , where the near wake flow is dominated by the shedding of Karman vortices. In this Reynolds number range, Goldstein (1938),  $C_{DN}$  is approximately constant (i.e. virtually independent of Reynolds number), taking a value of approximately 1.1. The Reynolds number independence was confirmed for this investigation, as shown in Fig. 6, over the Reynolds number range  $6 \times 10^4 \leq Re \leq 3 \times 10^5$ . However, it may be worth noting that the average value of  $C_{DN}$  in Fig. 6 is around 0.9 compared to the value of 1.1 found by Burnsall and Loftin (1951) at larger yaw angles up to  $90^\circ$ . This discrepancy was not investigated.

The average normal pressure coefficient,  $\overline{C}_{pN}$ , was also determined for the subcritical data presented in Fig. 6. These  $\overline{C}_{pN}$  results are shown in Fig. 7 plotted against  $Re_{sw}$ . Figure 7 shows that  $\overline{C}_{pN}$  is also independent of  $Re_{sw}$  for subcritical flows in the Reynolds number range investigated.

The subcritical  $\overline{C}_p$  versus  $\gamma$  data were isolated from Fig. 4 and presented as Fig. 8. Comparison of Figs. 4 and 8 shows that the variance of  $C_p$  at a given yaw angle for the subcritical flow data, Fig. 4, is much less than the variance of  $C_p$  for the combined data at the same yaw angle, Fig. 8. In Fig. 4, the apparent scatter is  $\pm 50\%$  while in Fig. 8, that has been reduced to  $\pm 5\%$ . Thus the subcritical  $\overline{C}_p$  versus  $\gamma$  dependence may be accurately predicted by a function of the form:

$$\overline{C}_p = \overline{C}_{p90^\circ} \sin^2 \gamma$$

where  $C_{p90^\circ}$  is a constant equal to the value of  $\overline{C}_p$  at 90 degrees yaw. The ability to fit the data with a  $\sin^2 \gamma$  function is consistent the predictions of inviscid sweepback theory.

An example of a transition range, laminar separation with turbulent reattachment, pressure profile is pictured in Fig. 9. This plot was taken for the medium nose cylinder in a 179 ft/sec flow at 15 degrees yaw. Here, the characteristic features are laminar separation peaks around  $\theta \approx 80$  and  $280$  degrees, followed by a smooth, relatively strong pressure recovery. Separation takes place at  $\theta \approx 120$  and  $240$  degrees. The renewed pressure recovery immediately after the laminar separation point is indicative of the reattachment of a turbulent boundary layer. As with Fig. 5, a potential theory  $C_p$  versus  $\theta$  profile is overplotted for comparison.

The  $Re_{sw}$  range in which transition range data were found was  $1.6 \times 10^5 \leq Re_{sw} \leq 3.3 \times 10^5$ . In the transition range, the boundary layer separation points move rearward as the Reynolds number increases allowing improved pressure recovery. This rearward movement of the separation point manifests itself in smaller drag coefficients and more negative  $\overline{C}_{pN}$ . The reduced  $C_{DN}$  results from the improved pressure recovery at the base  $\overline{C}_{pN}$  becomes smaller (i.e. more negative) because the minimum pressure peaks become lower as the separation points move rearward.

The trend toward decreasing  $C_{DN}$  is shown in Fig. 10 where the transition  $C_{DN}$  data are plotted against  $Re_{sw}$ . Data were obtained for both the short and medium nose cylinders at yaw angles from 10 to 20 degrees. Similar results can be found for  $\bar{C}_{pN}$  as seen in Fig. 11.

For a given cylinder, the precise Reynolds number where transition from a laminar boundary layer to a turbulent boundary layer takes place greatly depends upon the freestream conditions (e.g. the freestream turbulence level). This is because the instabilities in the cylinder boundary layer which amplify to cause turbulence are highly sensitive to disturbances. This sensitivity, combined with the inherently strong Reynolds number dependence of the transition flow regime, leads to the expectation of an increase in the deviation about the mean  $\bar{C}_p$  value at specific yaw angles for transition flows over the subcritical case.

The deviation about the mean value of  $\bar{C}_p$  for the transitional range data is as large as  $\pm 30\%$  for the 15 degree yaw case, as seen in Fig. 12. The data in Fig. 12 were obtained by isolating the transition range  $\bar{C}_p$  results shown in Fig. 4. This deviation cannot be entirely construed as scatter. For all three yaw angles shown,  $\bar{C}_p$  decreases with increasing freestream velocity (i.e. for increasing  $Re_{sw}$ ). Thus a substantial part of the deviation in the  $\bar{C}_p$  measurements is a manifestation of the Reynolds number dependence of the transitional flows.

The third class of flows, the supercritical range, corresponds to the latter part of the transition range, and beyond,

where the cylinder boundary layer is turbulent throughout. Separation is delayed until the flow has reached the leeward side of the cylinder resulting in a much higher pressure recovery at the base. An example of a supercritical  $C_{pN}$  versus  $\theta$  profile is plotted in Fig. 13 along with a potential solution profile.

In the range of  $Re_{sw}$  studied in this investigation, supercritical flows are highly Reynolds number dependent. At the low end of the supercritical range,  $Re_{sw} = 3 \times 10^5$ ,  $C_{DN}$  continues to decrease with increasing  $Re_{sw}$ . Roshko (1961) determined that,  $C_{DN}$  will reach a minimum and subsequently rebound to some intermediate value, 0.7, and remains constant up to  $Re_{sw} = 10^7$ .

This investigation was only able to study the supercritical range up to the vicinity where the minimum  $C_{DN}$  value is reached. This corresponds to a Reynolds number of approximately  $7 \times 10^5$ . These results, showing the continued roll-off of  $C_{DN}$  with  $Re_{sw}$ , are presented as Fig. 14. Most of these data were taken at a 10 degree yaw angle.  $\bar{C}_{pN}$  also continues to decrease with increasing  $Re_{sw}$  which is illustrated in Fig. 15.

Because only one yaw angle is well represented in the supercritical data, not much new information can be gleaned from the  $\bar{C}_p$  versus  $\gamma$  plot shown in Fig. 16. However, for each cylinder, the 10 degree yaw angle data is ordered, decreasing with increasing freestream velocity. This is consistent with the trend observed in the transition range plot, Fig. 12, which led to the conclusion that much of the variation of  $\bar{C}_p$  at a given  $\gamma$  is an indication of the Reynolds number effect on  $\bar{C}_{pN}$  and  $C_{DN}$ .

The work presented thus far, confirms what has been already reported in the literature. Three classes of flow have been

identified according to the shape of the  $C_{pN}$  versus  $\theta$  profiles. Further, these classes have been shown to coincide with the flow regimes identified for flow over a cylinder aligned perpendicular to the flow.

Idealized sketches of  $C_{pN}$  versus  $\theta$  profiles for the three different ranges are shown in Fig. 17. These plots were obtained by sketching the three curves presented in Figs. 5, 9, and 13. While Fig. 17 is not quantitatively exact, the general features and relative proportions are correct.

In general, the magnitude of the minimum pressure peak will be smaller for the laminar separation, subcritical range, flows than for the transitional and supercritical flows, see Fig. 17(a). Further, the pressure recovery will be much less. This means that both  $C_{DN}$  and  $\bar{C}_{pN}$  will be highest in subcritical flows. Because there is little variation of  $\bar{C}_{pN}$  with  $Re_{sw}$  in the subcritical range,  $\bar{C}_p$  varies only with  $\gamma$  following a relation of the form

$$\bar{C}_p = \bar{C}_{p90^\circ} \sin^2 \gamma$$

In transitional flows, laminar separation with turbulent reattachment, Fig. 17(b) the minimum pressure peak is lower than in the laminar separation case. However, turbulent reattachment allows a greater pressure recovery on the leeward side of the cylinder. Therefore, the absolute values of  $C_{DN}$  and  $\bar{C}_{pN}$  are smaller and larger respectively in transitional flows than in subcritical flows; both  $C_{DN}$  and  $\bar{C}_{pN}$  are lower than the subcritical values.

A turbulent separation profile is pictured in Fig. 17(c). Here the minimum pressure peaks are very smooth and have moved rearward to the  $\theta = 90$  and  $270$  degree positions. A very strong pressure recovery takes place because the boundary layer is still attached on the leeward side. Thus,  $C_{pN}$  and  $C_{DN}$  are even lower in supercritical than in transitional flows.

#### 4.3 Asymmetric $C_{pN}$ Profile

During the course of this investigation, an additional type of  $C_{pN}$  versus  $\theta$  profile was observed. The startling feature of this type of profile is the asymmetry about the horizontal plane of symmetry. One reason that these profiles were only recently discovered, Yanta and Wardlaw (1981), is that in earlier studies, symmetric profiles were assumed a priori; local pressure measurements were made only between  $\theta = 0$  and  $\theta = 180$  degrees. With only half of the profile, the asymmetry could not be seen.

Examples of the asymmetric profiles are shown in Figs. 18 and 19. The profile in Fig. 18 was taken from the medium nose cylinder in 114 ft/sec flow at a yaw angle of 17.5 degrees. Figure 19 was generated from data taken from the same cylinder in 61 ft/sec flow with 15 degree yaw. It was initially believed that the asymmetric profiles represented a new Reynolds number regime characteristic of flow over yawed cylinders. However, the work of Allen and Perkins (1951), and more recently, Thomson and Morrison (1971) leads to a more plausible explanation of the phenomenon.

Thomson and Morrison (1971) reported that, for cylinders yawed up to 60 degrees, the cylinder near wake is dominated by an

attached vortex street phenomenon. Each vortex in the street is formed by the coalescence of the boundary layer vorticity as the boundary layer is swept off the leeward side of the cylinder. These vortices shed alternately from side to side along the length of the cylinder and extend into the freestream at some angle to the cylinder axis. The angle each vortex makes with the cylinder axis is dependent upon the yaw angle and the freestream velocity. At yaw angles greater than 60 degrees, the vortices shed parallel to the cylinder and a Karman vortex street ensues.

When Karman vortices are shed from the cylinder, the vortices shed alternately from top and bottom. If pressure measurements are averaged over a sufficiently long period of time, the effect of individual vortices will be eliminated and the  $C_{pN}$  versus  $\theta$  profile will be symmetric about the horizontal plane through  $\theta = 0$  degree. However, for a given set of flow conditions, the locations where attached vortices are shed, along the cylinder axis, were found to be very stable. This stability was established by shaking the cylinder using the yaw control and verifying that the profile shape did not change. At any of these locations, the mean pressure distribution on the top half of the cylinder will be grossly different from the distribution on the bottom half. This difference will not change much with longer sampling times because the flow is so stable. Thus, it is believed that asymmetric pressure profiles occur when the measuring station location coincides with the axial location of the shedding of an attached vortex.

Evidence supporting the conclusion that asymmetric profiles do not comprise a fourth Reynolds number regime can be found in Fig. 20. In this plot, all three cylinders are represented over a Reynolds number range of  $10^5 \leq Re_{sw} \leq 1.3 \times 10^6$ . Since this range virtually spans the entire range covered in this investigation, asymmetric flows clearly are not a separate regime.

Two important features of Fig. 20 are the large values of  $C_{DN}$  and the sudden drop in  $C_{DN}$  at  $Re_{sw} \approx 2 \times 10^5$ . The overall high level of  $C_{DN}$  indicates little pressure recovery on the leeward side of either the top or bottom half of the cylinder. This may be seen in Figs. 18 and 19.

The sudden drop in  $C_{DN}$  indicates an increase in the average base pressure, possibly resulting from a change in the strength of the attached vortices at the Reynolds number,  $2 \times 10^5$ . It is perhaps noteworthy that the drop in  $C_{DN}$  coincides with the onset of the transition range. If this occurrence were not fortuitous, then it would seem that the strength of the attached vortices may be affected by the type of boundary layer separation.

Figure 21 is a plot of  $\bar{C}_{pN}$  as a function of  $Re_{sw}$  for the asymmetric profile data. Here  $\bar{C}_{pN}$  is much lower than in the subcritical, transitional, and supercritical ranges. This is again indicative of low minimum pressure peaks and weak pressure recoveries at the base.  $\bar{C}_{pN}$  increases very strongly with  $Re_{sw}$  going from a minimum value of  $-0.88$  at  $Re_{sw} \approx 10^5$  to a maximum around  $-0.25$  at  $Re_{sw} \approx 10^6$ . Much of the increase in  $\bar{C}_{pN}$  occurs around  $Re_{sw} = 2 \times 10^5$  which is consistent with the results shown in Fig. 20.

As with the other three types of  $C_{pN}$  versus  $\theta$  profiles, the  $\bar{C}_p$  versus  $\gamma$  results were plotted for asymmetric flows, and are presented in Fig. 22. Here the deviation about the mean value of  $\bar{C}_p$  at a given  $\gamma$  is approximately  $\pm 10\%$ . Contrary to previous results, the higher freestream velocity data lie above the lower velocity data. However, this is to be expected since  $\bar{C}_{pN}$  increases with  $Re_{sw}$  whereas in transitional and early supercritical flows  $\bar{C}_{pN}$  decreased with  $Re_{sw}$ . Therefore, for all four classes of flow, the apparent scatter in the  $\bar{C}_p$  results for a particular yaw angle is largely a manifestation of the Reynolds number influence.

Over the Reynolds number range investigated the absolute magnitudes of  $C_{DN}$  and  $\bar{C}_{pN}$  are larger for the asymmetric flows than for the other three regimes. This is caused by low minimum pressure peaks and weak or non-existent pressure recoveries on the leeward side of the cylinder. It is clear, when comparing Figs. 18-21 with similar plots in Section 4.2, that the flow field in the vicinity of an attached vortex is radically different from the mean flow field in the wake of a 90 degree yawed cylinder. The attached vortex phenomenon will greatly affect engineering situations where  $\bar{C}_{pN}$  and/or  $C_{DN}$  along yawed high aspect ratio bodies of revolution are important parameters.

#### 4.4 Discussion of 5-30 Degree Results

After categorizing the flow past a yawed cylinder for moderate to large yaw angles, the next step is to examine the combined results. The purpose is to look for trends which

describe the behavior of the average pressure coefficient over a large Reynolds number range.

Figure 23 is a composite plot of the  $C_{DN}$  results presented in Section 4.2 excluding the long nose cylinder results. Data from the report of Bursnall and Loftin (1951) have been copied onto Fig. 23 for comparison. These data appear as points that are half solid and half open.

The primary feature of Fig. 23 is the apparent high correlation between various sets of data. For instance, there appears to be a correlation between the short and medium nose cylinder results, indicating internal consistency within this investigation. More interestingly, there appears to be a similarity between the present data and Bursnall and Loftin's data. This correlation, if true, would support the current belief that the  $C_{DN}$  and  $\bar{C}_{pN}$  dependences on  $Re_{sw}$  for yawed cylinders are identical to the 90 degree yaw dependences. Further, this correlation would imply that  $\bar{C}_p$  and  $C_D$  could be found for known yaw angle and freestream velocity, using inviscid sweepback theory and the 90 degree yaw  $\bar{C}_p$  versus  $Re$  and  $C_D$  versus  $Re$  curves. The only restriction on the application of sweepback theory would be that the associated  $C_{pN}$  versus  $\theta$  profile can be categorized into either the subcritical, transitional, or supercritical ranges.

It is important to note that, here, the word "correlation" is used to mean qualitative similarity between the slopes of two or more regression lines. A moderate shift in the intercept of the regression lines is acceptable because of the Reynolds number sensitivity of the transition range. The stricter statistical definition of correlation was found not to be very useful in this

case because the effectiveness of statistical correlation of regression slopes, covariance analysis, is limited by the deviation of the data about a lumped regression line. For these data, the deviation is large, and correlation will probably be concluded at a high level of significance. However, because of the large variability, the correlation conclusion is not very informative. Therefore, the more general sense of qualitative correlation was deemed sufficient in this discussion.

To verify the correlation of data sets, linear regression lines were fitted through the short nose data, the medium nose data, Bursnall and Loftin's (1951) combined 30 and 45 degree yaw data, and through Bursnall and Loftin's lumped 60 and 75 degree yaw data. The regression analysis included only subcritical, transitional, and supercritical data which fell in the Reynolds number range,  $2 \times 10^5 \leq Re_{sw} \leq 10^6$ . The two 30 degree yaw Bursnall and Loftin points,  $C_{DN} = 1.350$  and 1.325, were assumed to have asymmetric type profiles and were not included in the regression fitting. No attempt was made to rigorously verify the linearity of the data sets.

The reason for splitting Bursnall and Loftin's data into two sets is that, according to Thomson and Morrison (1971), the flow field in the wake of the cylinder changes from an attached vortex field to a Karman vortex street wake as yaw angle increases beyond 60 degrees. However, according to Allen and Perkins (1951), Lamont and Hunt (1971), and others, the change in wake flow field does not affect  $\bar{C}_{pN}$  or  $C_{DN}$ . This latter contention can be tested by splitting the Bursnall and Loftin data and comparing the regression lines of the two subsets.

Three of the regression lines are shown in Fig. 24. The solid line is the regression line of the lumped Bursnall and Loftin 60 and 75 degree yaw data. The equation of the line is:

$$C_{DN} = 13.4 - 2.29 Re_{sw}$$

The short and medium nose regression lines appear as broken lines. The medium nose line is broken by two dots and lies above the short nose line in Fig. 24. The equations of these lines are:

$$C_{DN} = 5.45 - 0.868 Re_{sw}$$

and

$$C_{DN} = 6.76 - 1.08 Re_{sw}$$

for the short and medium nose data respectively. Along with these three lines, a portion of the 90 degree yaw  $C_{DN}$  versus  $Re$  curve, shown as a dashed line, is included in Fig. 24 for comparison.

Clearly the Bursnall and Loftin line is much steeper than the two other lines. This difference will be addressed in later paragraphs. The noteworthy feature of Fig. 24 is that the Bursnall and Loftin regression line falls virtually on top of the 90 degree yaw curve. This coincidence confirms the validity of using sweepback theory for cylinders yawed at angles greater than 60 degrees.

In Fig. 25, the short and medium nose regression lines are plotted along with the line through the lumped Bursnall and Loftin 30 and 45 degree data. As in Fig. 24, the Bursnall and Loftin fit is shown as a solid line while the short and medium nose lines appear as broken solid lines. The equation for the

Bursnall and Loftin line was found to be:

$$C_{DN} = 5.19 - 0.771 Re_{sw}$$

The correlation coefficient for this line is only - 0.665 while it is - 0.973 and - 0.993 for the short and medium nose cylinder lines, respectively.

In presenting Fig. 24, it was pointed out that the short and medium cylinder lines appeared to be different from the larger yaw angle line of Bursnall and Loftin. While the Bursnall and Loftin line correlated extremely well to the 90 degree yaw curve, this was not the case for the other two lines. Now in Fig. 25, it can be seen that the Bursnall and Loftin lower yaw angle line agrees very well with the two lines from the present investigation. If this be the case, then apparently for yaw angles smaller than 60 degrees, the functional dependence of  $C_{DN}$ , and hence also  $\overline{C}_{pN}$ , on  $Re_{sw}$  will change with the changing wake flow field. This directly contradicts the literature which concluded no change in  $C_{DN}$  and  $\overline{C}_{pN}$  dependences with the change from the Karman vortex street to the attached vortex wake.

Inviscid sweepback theory still seems to be appropriate in the lower yaw angle cases. This is evidenced by the fact that application of sweepback theory still collapses the different yaw angle data onto a single line for each cylinder even at yaw angles as low as 5 degrees. However, the conclusion drawn in the preceding paragraph, that the  $C_{DN}$  and  $\overline{C}_{pN}$  dependences change with changing wake flow field, implies that, for the smaller yaw angles, characteristic attached vortex  $C_{DN}$  and  $\overline{C}_{pN}$  curves must be found to which the sweepback theory formula may be applied.

The lumped  $\bar{C}_{pN}$  versus  $Re_{sw}$  data are plotted in Fig. 26. This figure also includes the long nose,  $L/D = 100$ , cylinder data. Unfortunately, very little work has been done on  $\bar{C}_{pN}$  in the past, and there are no available published data for comparison.

However, the base pressure, the pressure behind the cylinder, has drawn much attention because of the belief that the oscillating base pressure is the generating mechanism for Karman vortices. Roshko (1961) defines a base pressure coefficient for a 90 degree yaw cylinder,  $\bar{C}_{pB}$ , as the average of the local pressure coefficients within a few degrees of  $\theta = 180$  degrees. For qualitative purposes,  $\bar{C}_{pB}$  can be directly compared to  $\bar{C}_{pN}$  because the shape of the  $C_{pN}$  versus  $\theta$  pressure profile on the windward side of the cylinder up to the separation points does not change much regardless of Reynolds number. Thus, the only changes in  $\bar{C}_{pN}$  result from variations in the base pressure.

Trend lines were drawn through the short and medium nose  $\bar{C}_{pN}$  data and are presented in Fig. 27. Roshko's (1961) 90 degree yaw  $\bar{C}_{pB}$  curve was reproduced in the figure for comparison. The medium nose trend line appears as a solid line. The broken solid line represents the trend in the short nose data, and Roshko's curve appears as a dashed line. Note that if Roshko had determined  $\bar{C}_{pN}$  rather than  $\bar{C}_{pB}$ , the inclusion of the minimum pressure peaks would have lowered his curve closer to where the present data lie.

Two observations can be made about Figs. 25 and 26. Firstly, the shape of the short and medium nose  $\bar{C}_{pN}$  trend lines

differ from the Roshko line. Yet the short and medium nose lines tend to be self consistent in shape. This supports the conclusion that the  $\overline{C}_{pN}$  dependence on  $Re_{sw}$  changes with changing wake flow field. Secondly, there appears to be a quantitative bias from the short nose data to the medium and long nose data; the short nose data are higher than the data from the other two cylinders. This discrepancy might be the result of the use of the music wire support system on the longer two cylinders. On the other hand, the discrepancy might be indicative of a cylinder nose length effect. It was not possible to isolate a probable cause for the shift on  $\overline{C}_{pN}$  for different cylinders. This problem must be resolved by more controlled experiments.

#### 4.5 Small Yaw Angle Results

The final study in this investigation was the attempt to determine a lower limit, below which the attached vortex street wake cannot be found. In this limit, it is believed that the cross-flow will be so weak that the axial boundary layer will dominate the near cylinder flow field along the entire length of the cylinder.

Allen and Perkins (1951) showed that the near wake flow field along the length of a yawed cylinder is qualitatively analogous to the flow around an impulsively started cylinder. In the impulsively started cylinder case, a cylinder, initially at rest in a quiescent flow, is instantaneously set into motion at a constant velocity in a direction perpendicular to the cylinder axis; the direction of motion is considered to be in the horizontal plane. Shortly after motion has begun, a pair of

"start-up" vortices forms on the leeward side of the cylinder and move to points just behind the vertical plane of symmetry. The start-up vortex pair grows with time until the vortices completely fill the base region behind the cylinder. As the vortices grow even larger, one will be cast off into the wake. The other vortex will continue to grow until it too is shed from the cylinder. At this time and for all subsequent times, the flow over the cylinder will not be influenced by the residual effects of the onset of motion. The cylinder wake will be a Karman vortex street.

When comparing the impulsively started cylinder to the flow over a yawed cylinder, the length along the yawed cylinder, measured from the nose, is analogous to the time elapsed from the onset of motion of the impulsively started cylinder. Thus, positions upstream of the yawed cylinder correspond to times when the impulsively started cylinder is at rest. The nose tip of the yawed cylinder is analogous to the instant that impulsive motion begins, and there will be a one to one correspondence between the flow field at any axial location on the yawed cylinder, and the flow field at some instant of time in the evolution of flow around the impulsively started cylinder.

According to the impulsively started cylinder model, reduction of yaw angle and/or freestream velocity in the yawed cylinder case is equivalent to the reduction in the velocity of the impulsively started cylinder. Clearly, there is a velocity below which the flow around the impulsively started cylinder will not develop into a Karman vortex street. Then, in the yawed cylinder case, there will be a combination of yaw angle and

Reynolds number where the attached vortex street phenomenon will not arise. Below this limit, the near cylinder flow field will be dominated by the axial boundary layer. The consequence of particular relevance to this investigation is that the relationships between  $\bar{C}_p$ ,  $\bar{C}_{pN}$ ,  $C_{pN}$  and  $C_{DN}$ , on the one hand, and  $\theta$ ,  $\gamma$ , and  $Re_{sw}$ , on the other, established in Sections 4.2 and 4.3, will no longer be valid. This is illustrated in Figs. 28, 29, and 30.

The profile in Fig. 28 was acquired for 179 ft/sec flow over the medium nose cylinder at 5 degree yaw. While the shape of the profile is similar to the turbulent separation, profiles seen in Section 4.2, there are differences. Firstly the minimum pressure peaks are very low. Secondly there is a sharp corner in the profile after the pressure recovery. Thirdly, there is a hump in the base pressure at  $\theta = 180$  degrees. These three features lead to the speculation that the profile in Fig. 27 resulted when the measuring station coincided with the location of the start-up vortex pair. Pressure profiles at smaller yaw angles were very jagged and irregular, and had lost any similarity to the profiles presented in Section 4.2.

Figure 29, a  $C_{DN}$  versus  $Re_{sw}$  plot for the data which could not be categorized as subcritical, transitional, supercritical, or asymmetric, clearly illustrates that, for these small angles, the  $C_{DN}$  relations established in Sections 4.2 and 4.3 are no longer valid. The large values of  $C_{DN}$  arise from dividing by the square of a very small number,  $\sin \gamma$ . A similar plot for  $\bar{C}_{pN}$ , Figure 30, shows that the  $\bar{C}_{pN}$  relations also break down at small yaw angles. The break down in the  $C_{DN}$  and  $\bar{C}_{pN}$  relation-

ships is construed to be an indication that the near cylinder flow field is dominated by the axial boundary layer. The behavior of  $\overline{C}_{pN}$  at low yaw angles should be more extensively examined in a separate investigation.

Finally, it was observed that, for yaw angles of 10 degrees and greater, all of the data taken in this investigation indicated an attached vortex street dominated flow field. Below 5 degrees yaw, the cylinder near flow field was found to be axial boundary layer dominated. At 5 degrees yaw, examples of both attached vortex street and axial boundary layer dominated flow were found. Therefore, the transition from axial boundary layer dominated flow to attached vortex street flow appears to occur around  $\gamma = 5$  degrees.

## 5. CONCLUSIONS

The pressure around a yawed circular cylinder was measured using pressure transducer techniques. The results of this investigation, after critical evaluation, led to the following conclusions:

- ° the  $C_{DN}$  and  $\bar{C}_{pN}$  dependences on  $Re_{sw}$  are different for the attached vortex wake ( $5^\circ < \gamma < 60^\circ$ ) than for the Karman vortex street wake ( $\gamma > 60^\circ$ ).
- ° in the transition Reynolds number range ( $\sim 2 \times 10^5 < Re_{sw} < \sim 10^6$ ),

$$C_{DN} \propto \log_{10} (Re_{sw})^{-2.3}$$

for the Karman vortex wake.

- ° for the attached vortex wake,

$$C_{DN} \propto \log_{10} (Re_{sw})^{-1.0}$$

- ° provided the type of boundary layer separation is known (e.g. laminar, transitional, or turbulent),  $\bar{C}_p$  may be determined using a limited form of the inviscid sweepback theory.
- ° without prior knowledge of the type of separation, at any given yaw angle,  $\bar{C}_{pN}$  may vary from a mean value by as much as  $\pm 50\%$  (e.g. at  $\gamma = 15^\circ$ ,  $\bar{C}_{pN} = -0.6 \pm 0.22$ ).
- ° the lower yaw angle limit where the near wake flow field undergoes transition from attached vortex street dominated to axial boundary layer dominated is approximately  $5^\circ$ .

## REFERENCES

- Achenbach, E., 1968, "Distribution of local pressure and skin friction around a circular cylinder in cross-flow up to  $Re = 5 \times 10^6$ ," J. Fluid Mech. 34, pp. 625-639.
- Allen, H.J. and Perkins, E.W., 1951, "A study of the effects of viscosity on flow over slender inclined bodies of revolution," NACA Report 1048.
- Bursnall, W.J. and Loftin, L.K., 1951, "Experimental investigation of the pressure distribution about a yawed circular cylinder in the critical Reynolds number range," NACA Tech. Note 2463.
- Goldstein, S. (ed.), 1938, Modern Developments in Fluid Dynamics, Clarendon Press, London.
- Lamont, P.J., 1982, "Pressures around an inclined ogive cylinder with laminar, transitional, or turbulent separation," AIAA J. 20, pp. 1492-1499.
- Lamont, P.J. and Hunt, B.L., 1976, "Pressure and force distributions on a sharp-nosed circular cylinder at large angles of inclination to a uniform subsonic stream," J. Fluid Mech. 76, pp. 519-559.
- Oberkampf, W.L., Owen, F.K., and Shivananda, T.P., 1981, "Experimental investigation of the asymmetric body vortex wake," AIAA J. 19, pp. 1025-1032.
- Roshko, A., 1961, "Experiments on the flow past a circular cylinder at very high Reynolds number," J. Fluid Mech. 10, pp. 345-346.
- Sarpkaya, T., 1966, "Separated flow about lifting bodies and impulsive flow about cylinders," AIAA J. 4, pp. 414-420.
- Schlichting, H., 1979, Boundary Layer Theory, 7th ed., McGraw-Hill, New York.
- Thomson, K.D. and Morrison, D.F., 1969, "The spacing, position and strength of vortices in the wake of slender cylindrical bodies at large incidence," Australian W.R.E. Report HSA 25.
- Thomson, K.D. and Morrison, D.F., 1971, "The spacing, position and strength of vortices in the wake of slender cylindrical bodies at large incidence," J. Fluid Mech. 50, pp. 751-783.
- Wardlaw, A.B. and Yanta, W.J., 1982, "Multistable vortex patterns on slender, circular bodies at high incidence," AIAA J. 20, pp. 509-515.

Willmarth, W.W., Sharma, L.K., and Inglis, S., 1977, "The Effect of cross flow and isolated roughness elements on the boundary layer and wall pressure fluctuations on circular cylinders," The University of Michigan, Department of Aerospace Engineering Report 014439-01.

Yanta, W.J. and Wardlaw, A.B., 1981, "Flowfield about and forces on slender bodies at high angles of attack," AIAA J. 19, pp. 296-302.

FIGURES

Figure 1. Schematic diagram illustrating the component parts, assembly, and mounting of a cylinder.

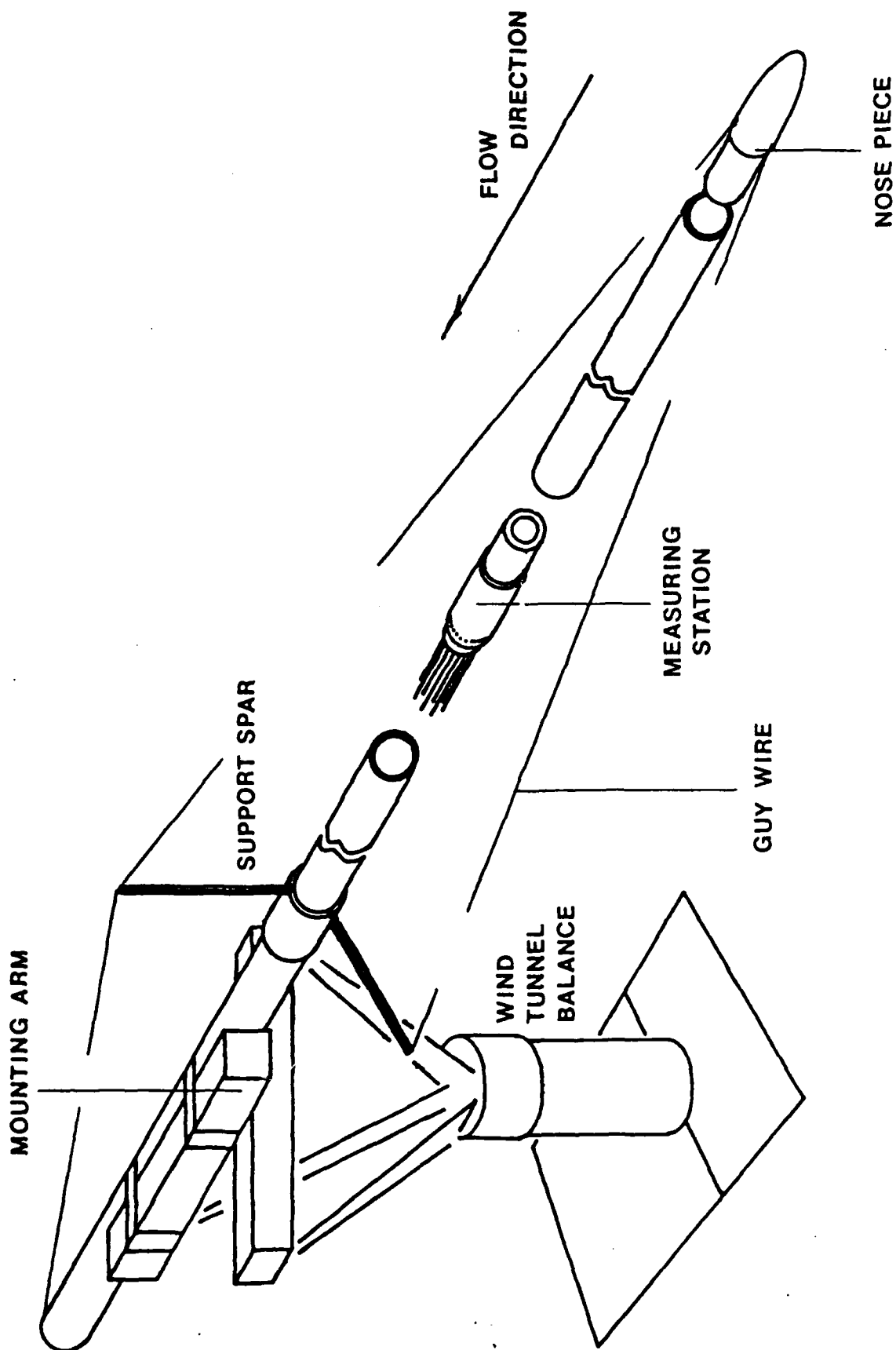


Figure 2. Schematic diagram showing the relative location and connection of the pressure sensing equipment.

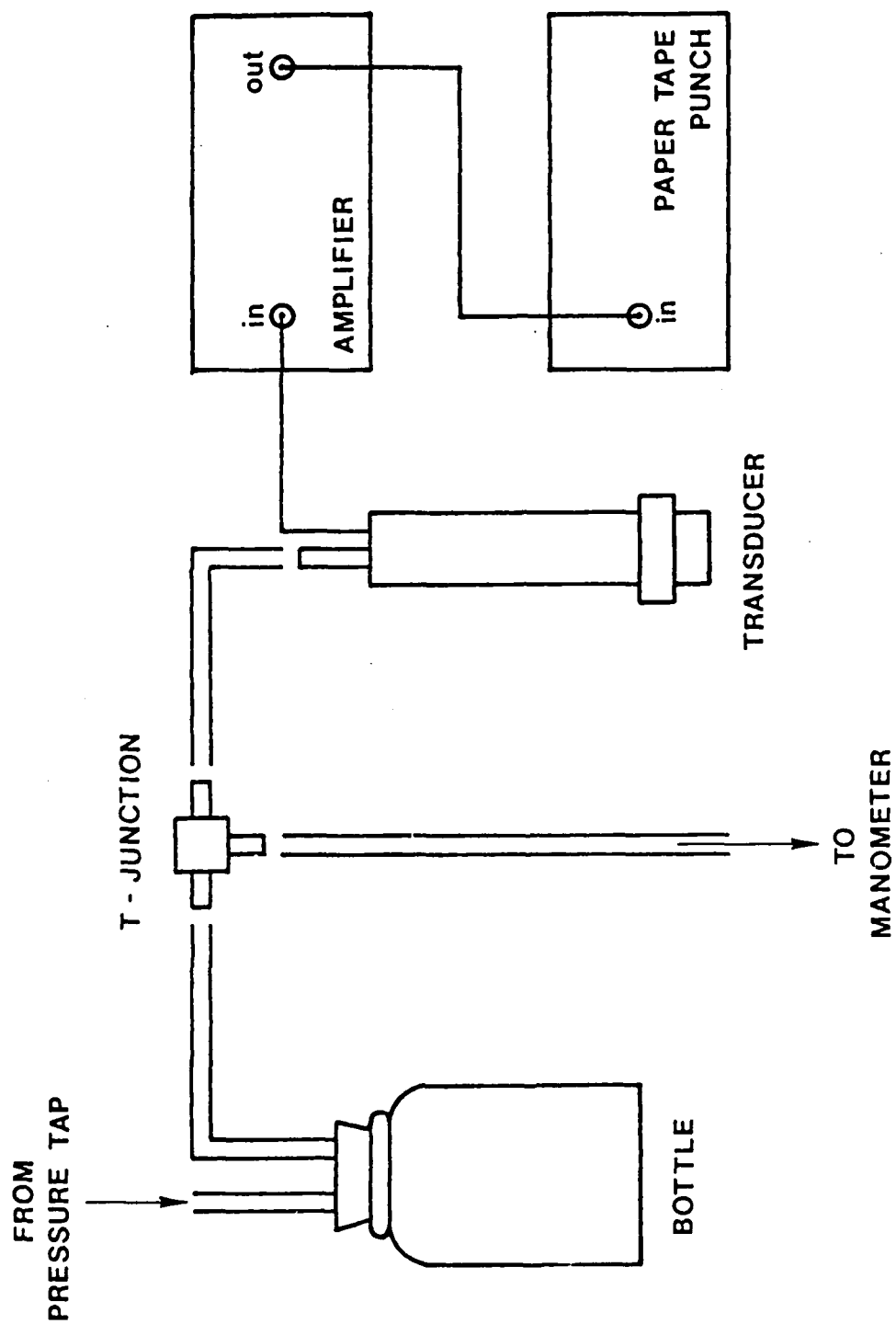


Figure 3. Schematic top-view diagram showing the mounted cylinder and the various flow parameters.

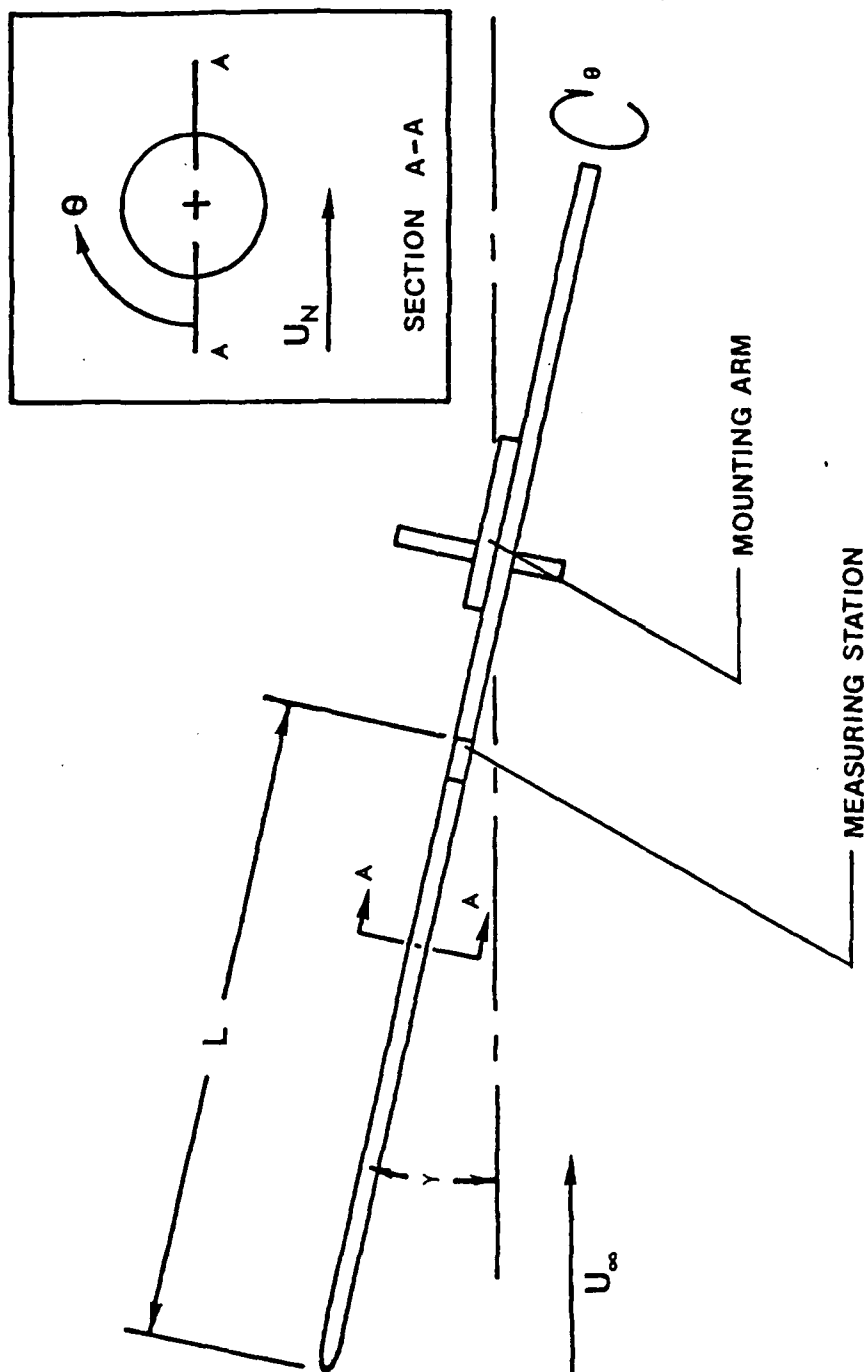


Figure 4. Combined plot of  $\bar{C}_p$  versus  $\gamma$  for all of the cases tested. The open symbols represent the  $L/D = 28$  data, solid points represent the  $L/D = 64$  data, and the two tone points represent the  $L/D = 100$  data. The symbols  $\circ$ ,  $\square$ ,  $\diamond$ ,  $\triangle$ , and  $\nabla$  correspond to velocities  $U_\infty = 61, 113, 147, 179, \text{ and } 223 \text{ ft/sec}$  respectively.

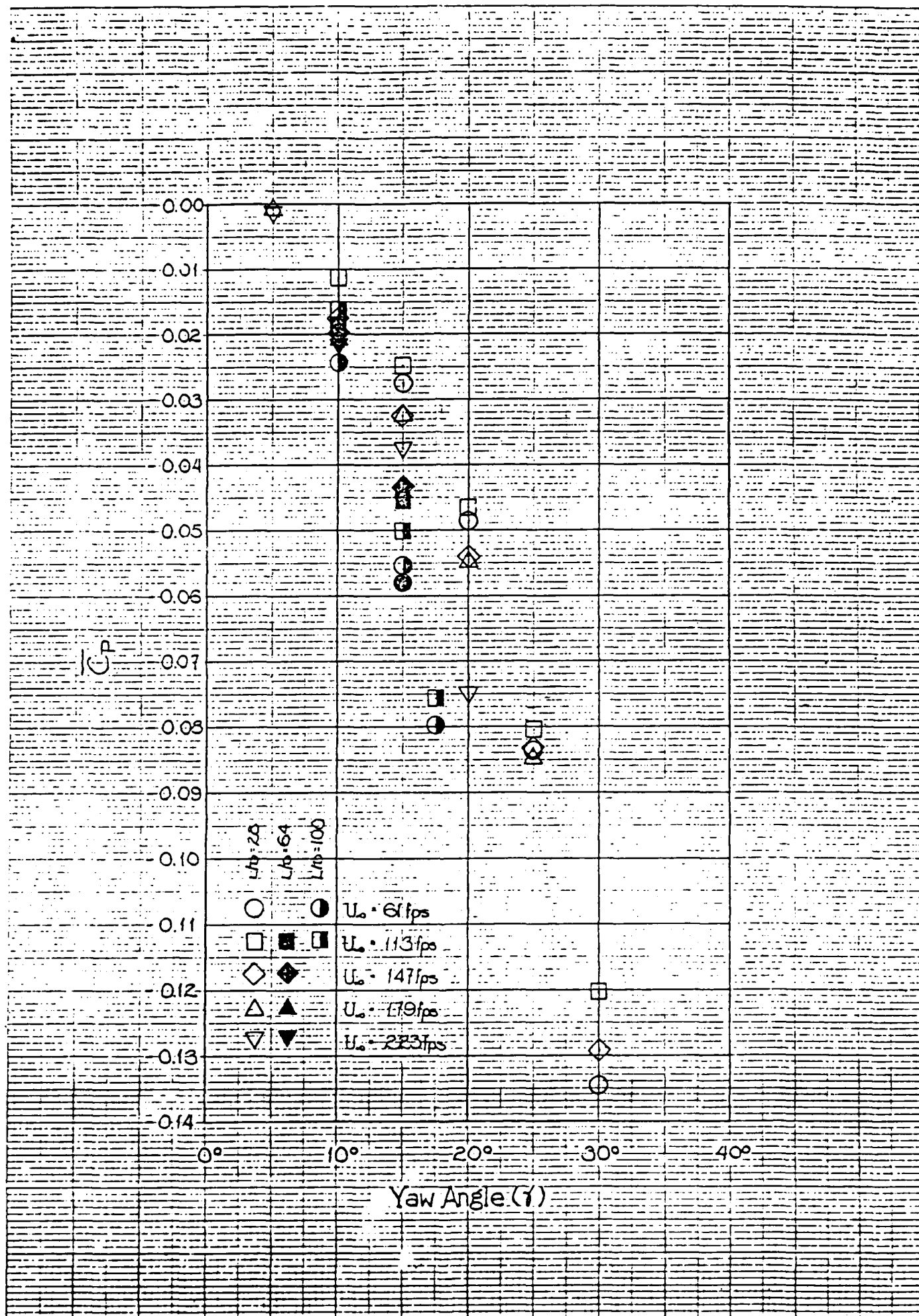


Figure 5. Representative example of a subcritical type of  $C_{pN}$  versus  $\theta$  profile. A potential solution curve is overplotted for comparison. The profile was taken at  $U_\infty = 148$  ft/sec,  $\gamma = 30^\circ$ , and  $L/D = 28$ .

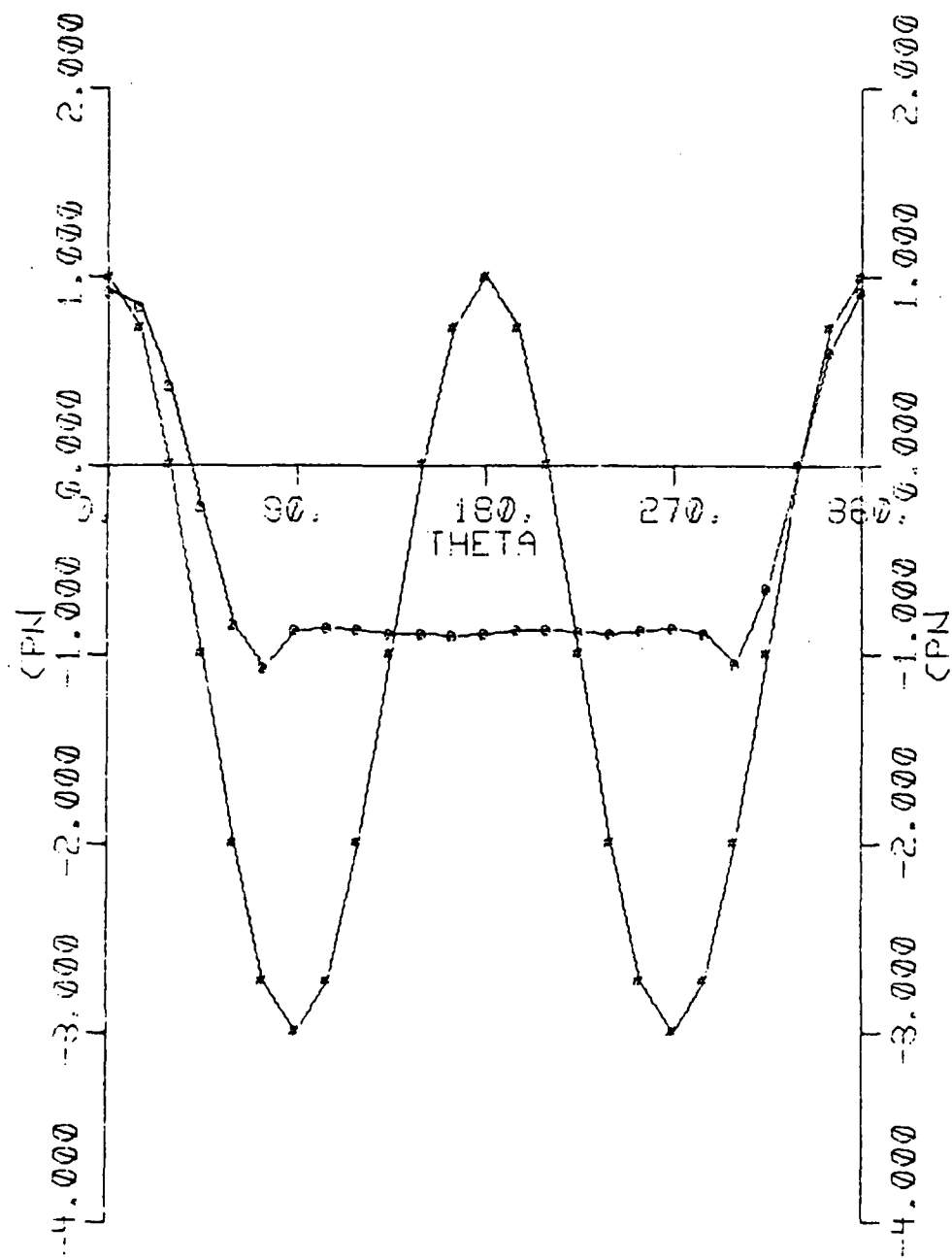


Figure 6. Plot of  $C_{DN}$  versus  $Re_{sw}$  for the laminar separation data. In all cases,  $L/D = 28$  with  $U_\infty$  varying from 60 to 180 ft/sec. The plot symbols  $\diamond$ ,  $\triangle$ ,  $\nabla$ , and  $\triangleleft$  represent yaw angles of  $15^\circ$ ,  $20^\circ$ ,  $25^\circ$ , and  $30^\circ$  respectively.

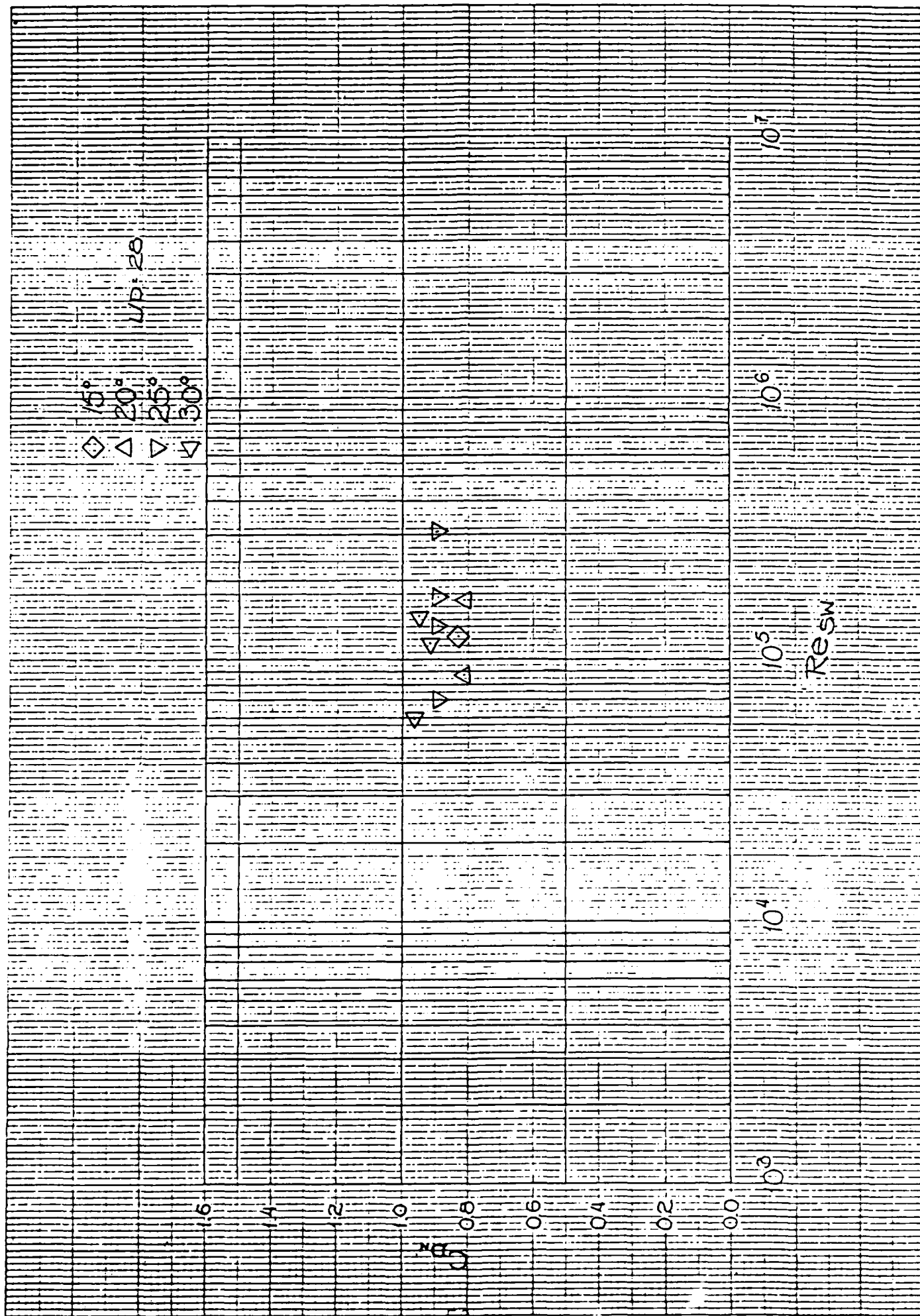


Figure 7. Plot of  $\bar{C}_{pN}$  versus  $Re_{sw}$  for the same sub-critical data plotted in Figure 6.

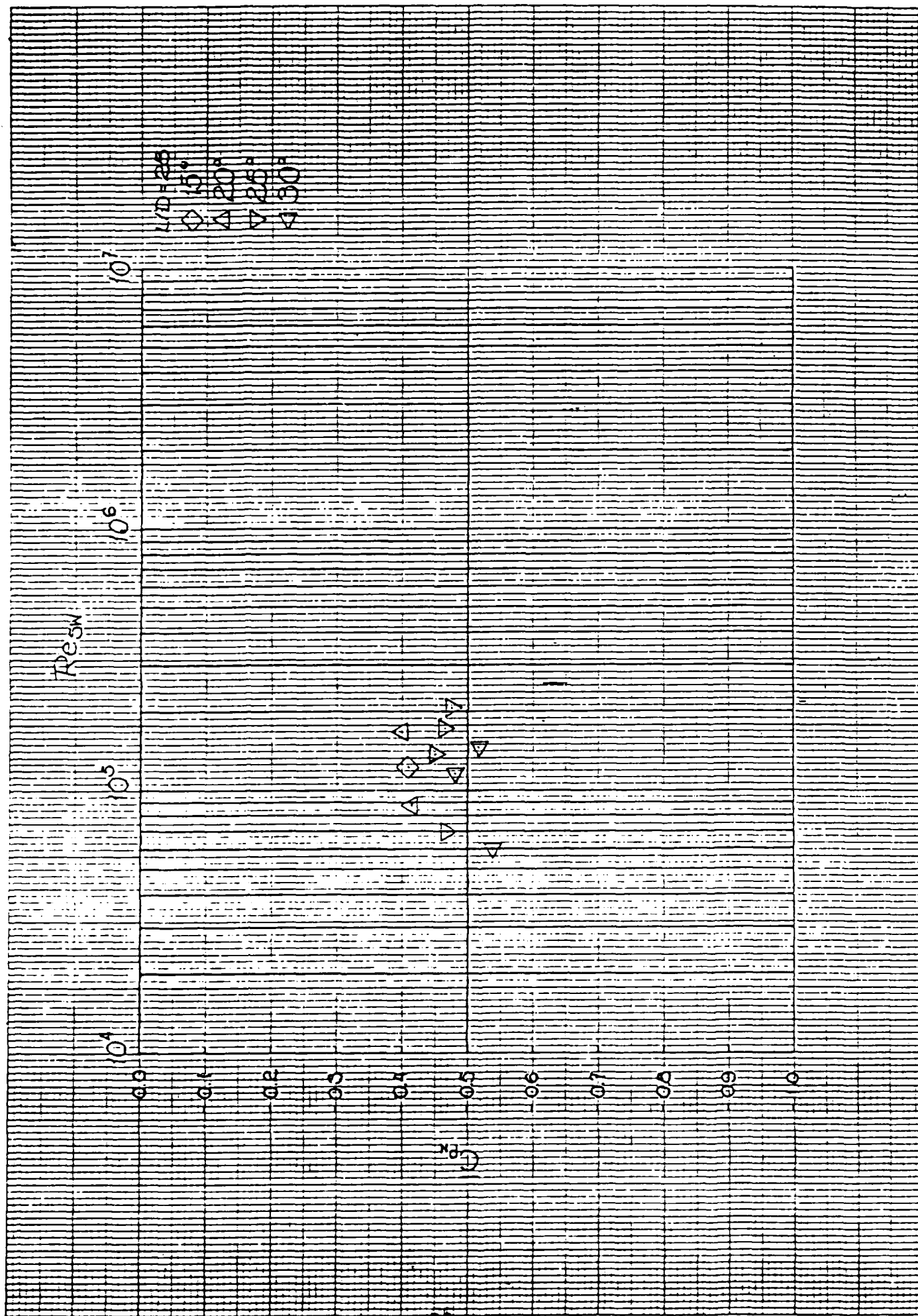


Figure 8. Isolated plot of  $\bar{C}_p$  versus  $\gamma$  for the sub-critical data shown in Figures 6 and 7. The symbols  $\bigcirc$ ,  $\square$ ,  $\diamond$ , and  $\triangle$  represent velocities,  $U_\infty = 61, 113, 147,$  and  $179$  ft/sec.

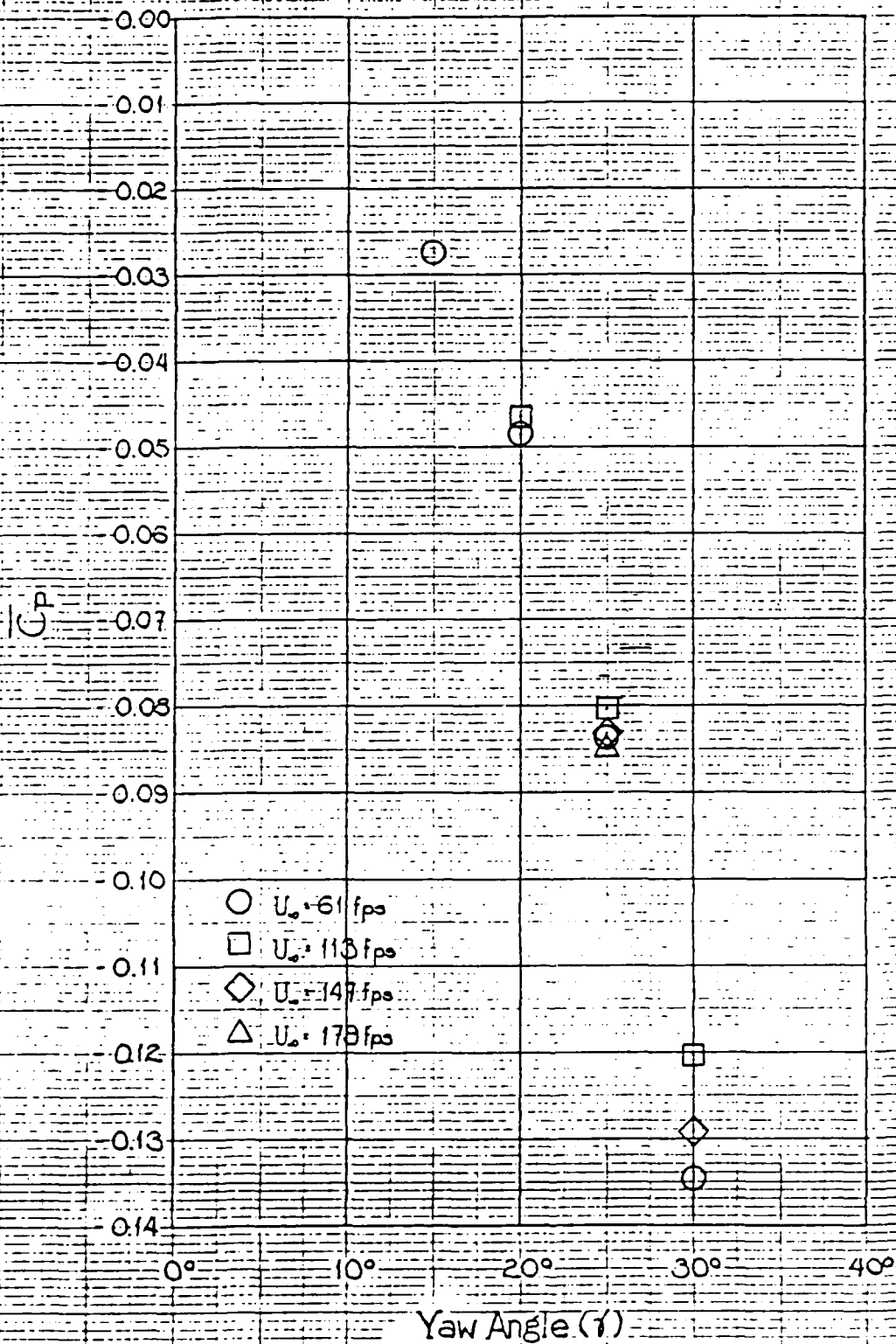


Figure 9. Representative example of a transitional type of  $C_{pN}$  versus  $\theta$  profile overplotted by a potential solution profile. This profile was taken at  $U_\infty = 179$  ft/sec,  $\gamma = 15^\circ$ , and  $L/D = 64$ .

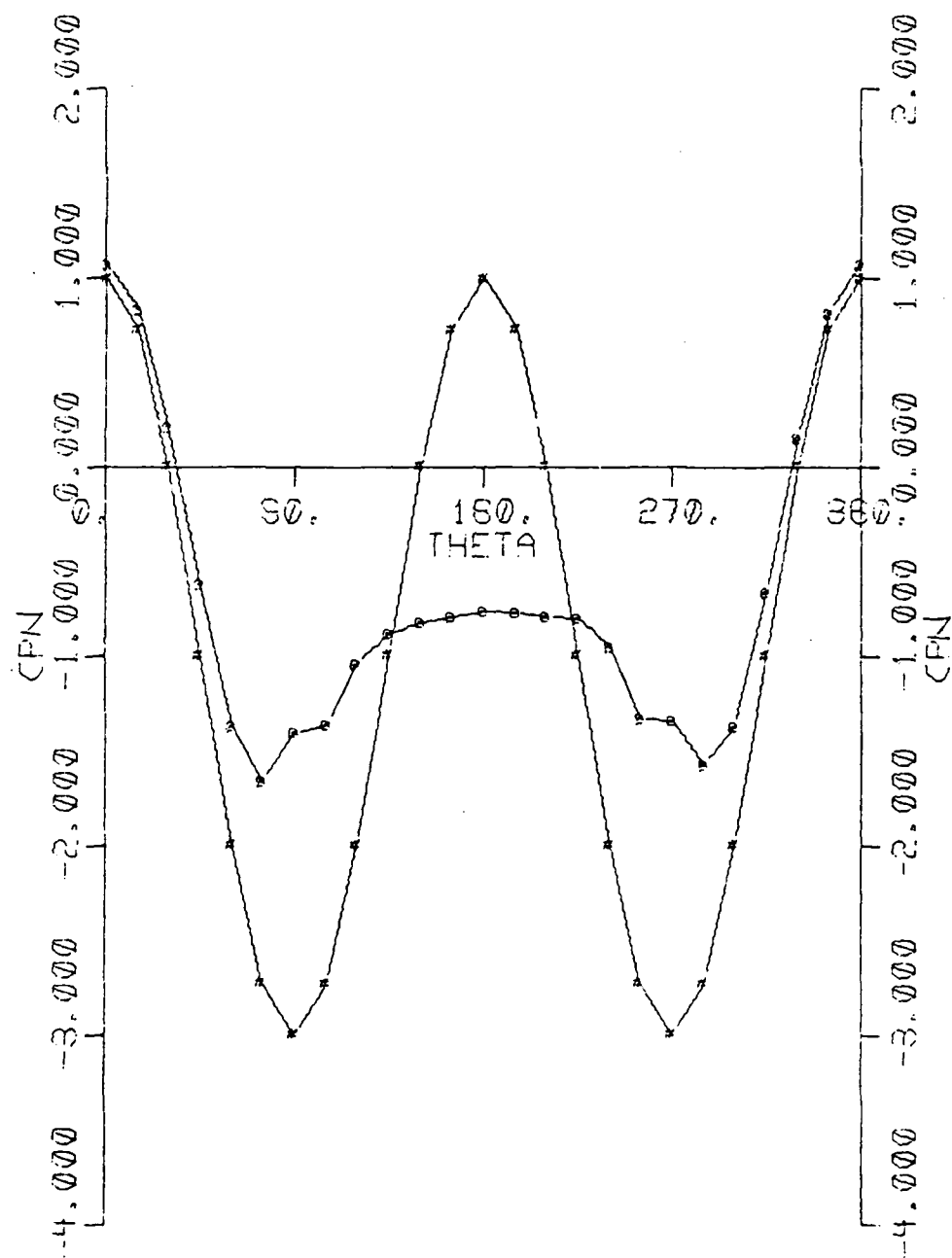
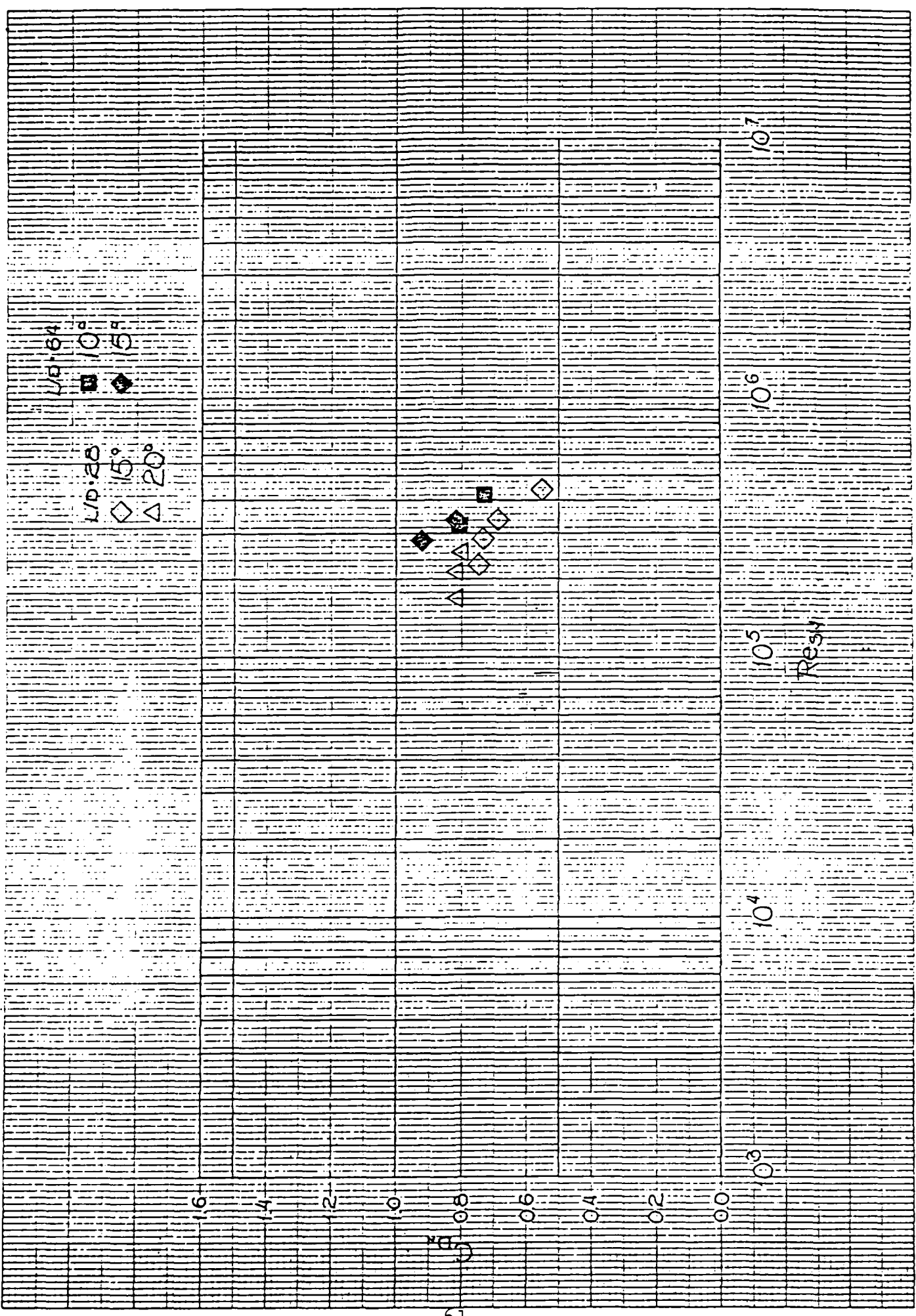


Figure 10. Plot of  $C_{DN}$  versus  $Re_{sw}$  for the transitional data. The solid points represent the  $L/D = 64$  data and the open points represent the  $L/D = 28$  data. The symbols  $\square$ ,  $\diamond$ , and  $\triangle$  correspond to  $\gamma = 10^\circ$ ,  $15^\circ$ , and  $20^\circ$  respectively.



Resv

Figure 11. Plot of  $\bar{C}_{pN}$  versus  $Re_{sw}$  for the same transitional data plotted in Figure 10.

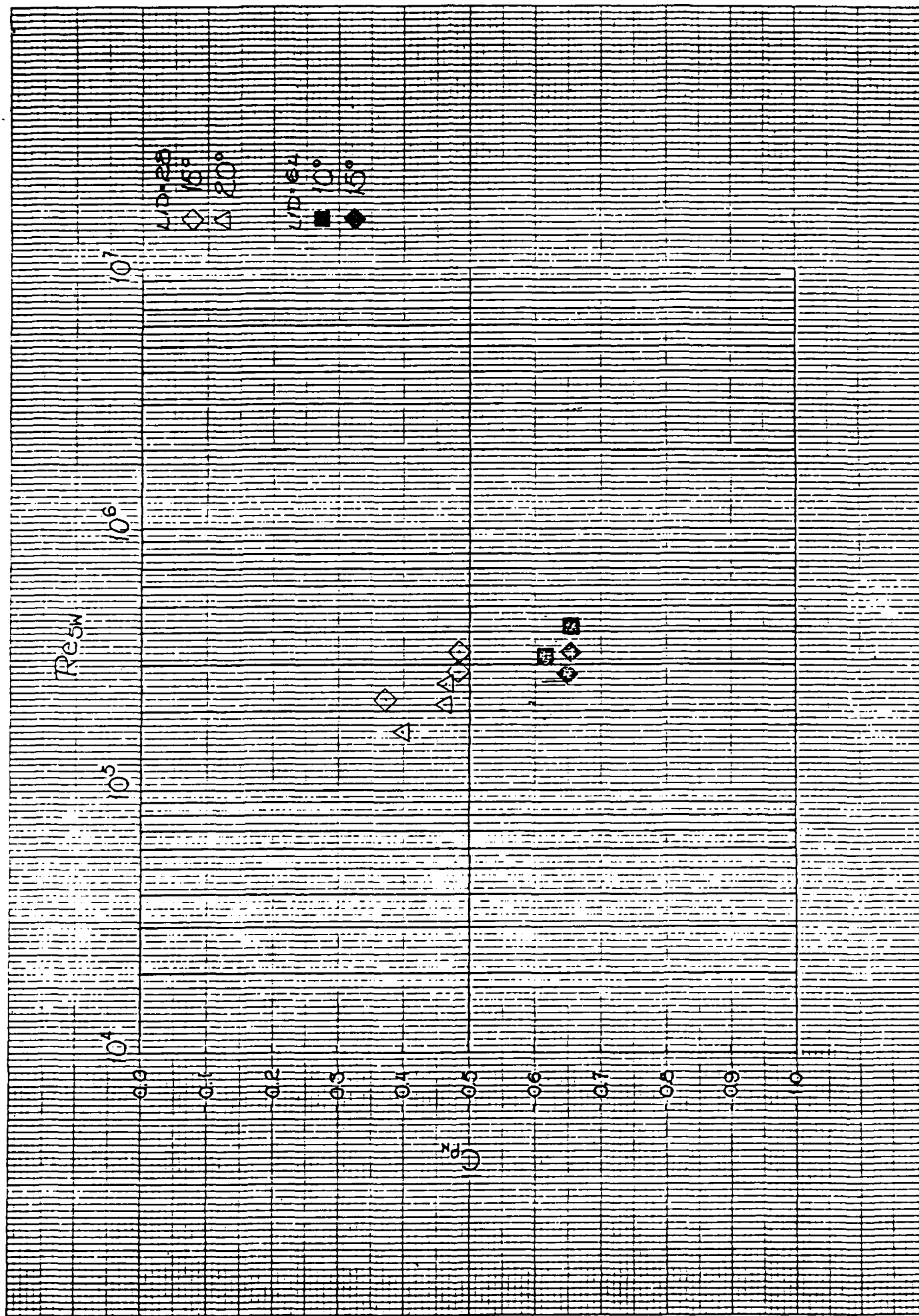


Figure 12. Isolated plot of  $C_p$  versus  $\gamma$  for the transitional data shown in Figures 10 and 11. The symbols  $\square$ ,  $\diamond$ , and  $\triangle$  correspond to  $U_\infty = 113, 147, \text{ and } 179 \text{ ft/sec.}$  Again, the open points represent the  $L/D = 28$  data and the solid points are for the  $L/D = 64$  data.

1303

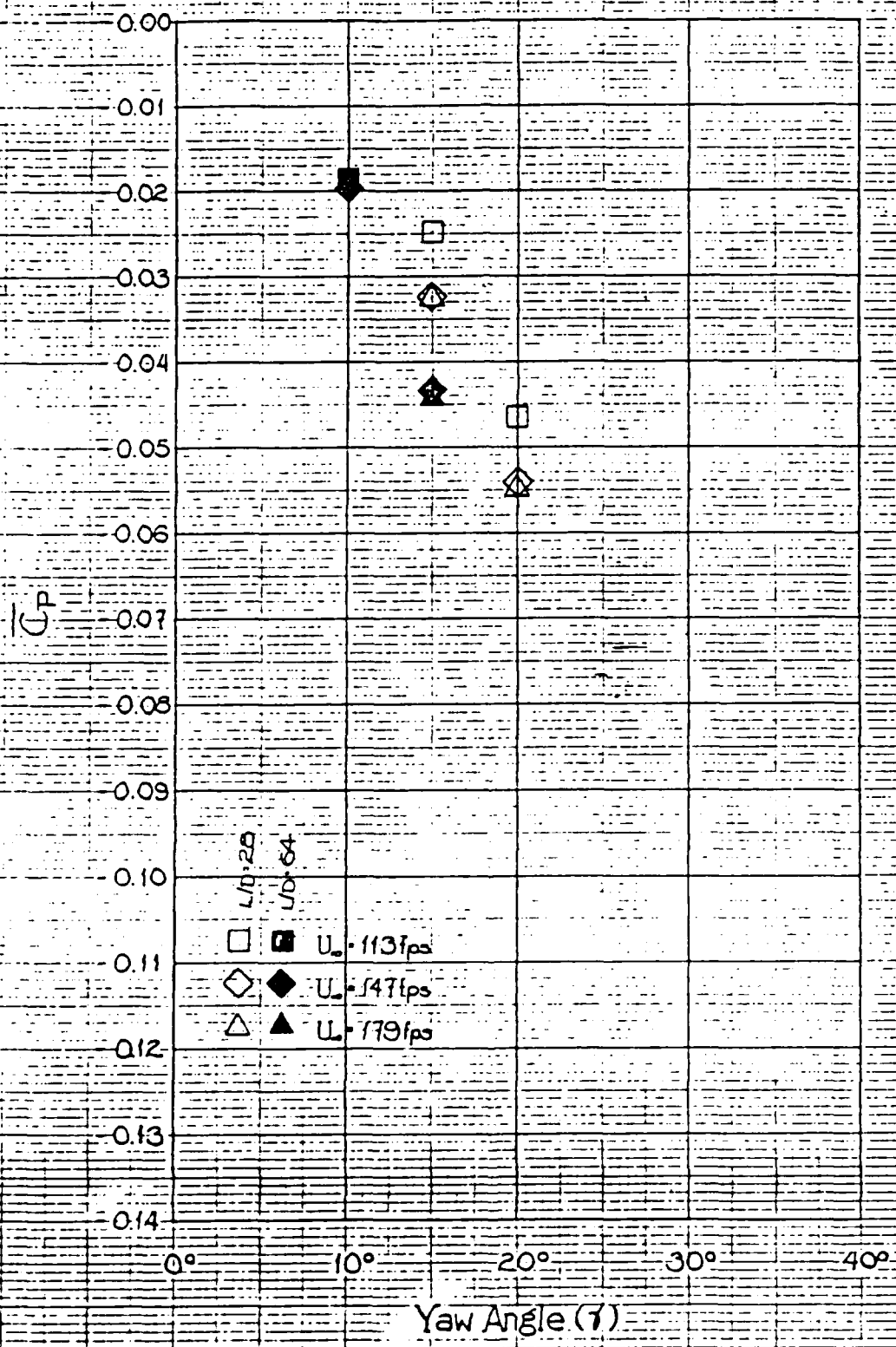


Figure 13. Representative example of a supercritical type of  $C_{pN}$  versus  $\theta$  profile overplotted with a potential solution profile. This profile was taken at  $U_\infty = 223$  ft/sec,  $\gamma = 10^\circ$ , and  $L/D = 28$ .

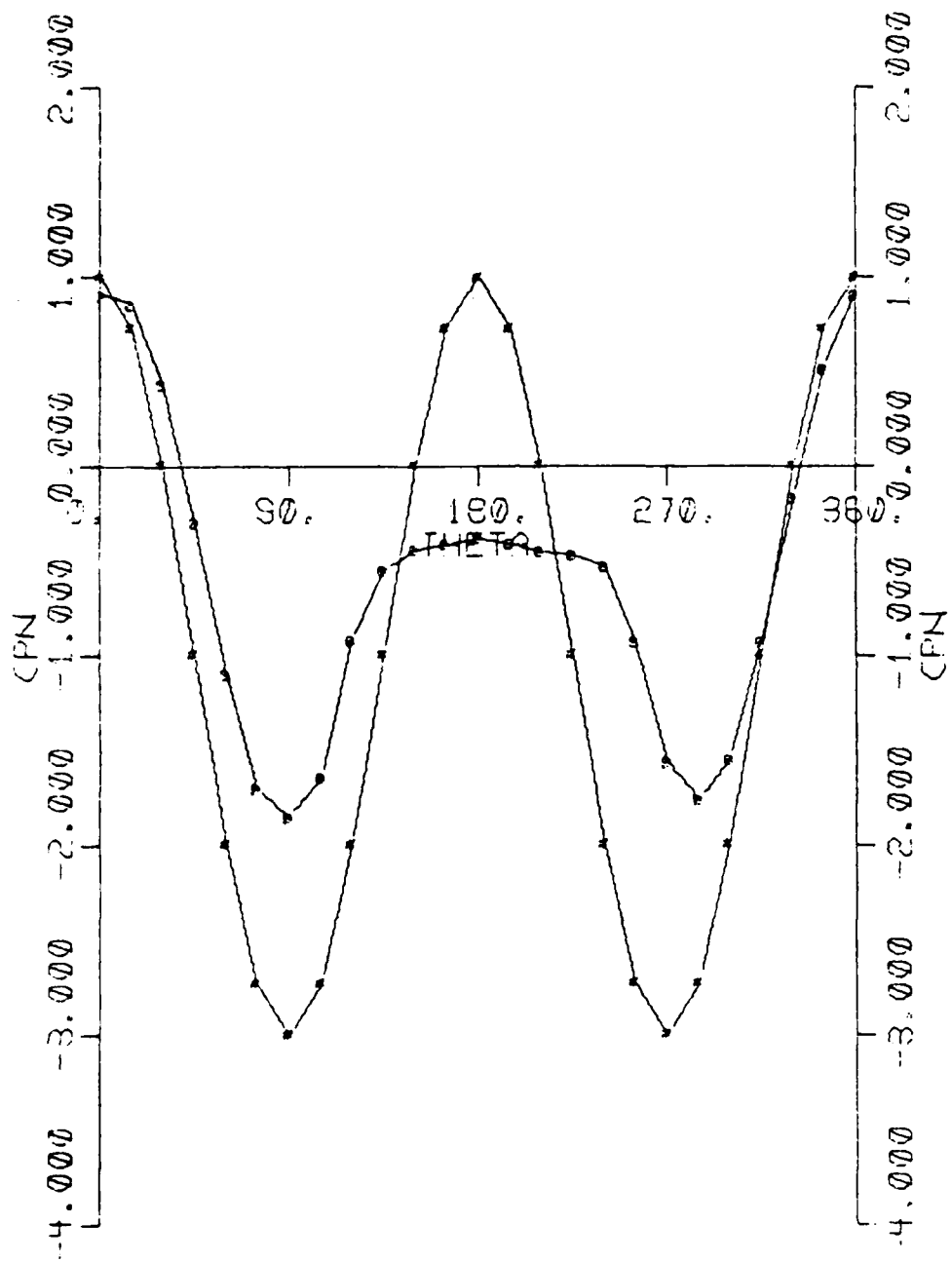


Figure 14. Plot of  $C_{DN}$  versus  $Re_{sw}$  for the supercritical data. The solid, open, and two tone points correspond to the L/D ratios of 64, 28, and 100 respectively. The  $\square$  shaped points represent the  $10^\circ$  yaw case, and the  $\diamond$  shaped points correspond to the  $15^\circ$  yaw case.

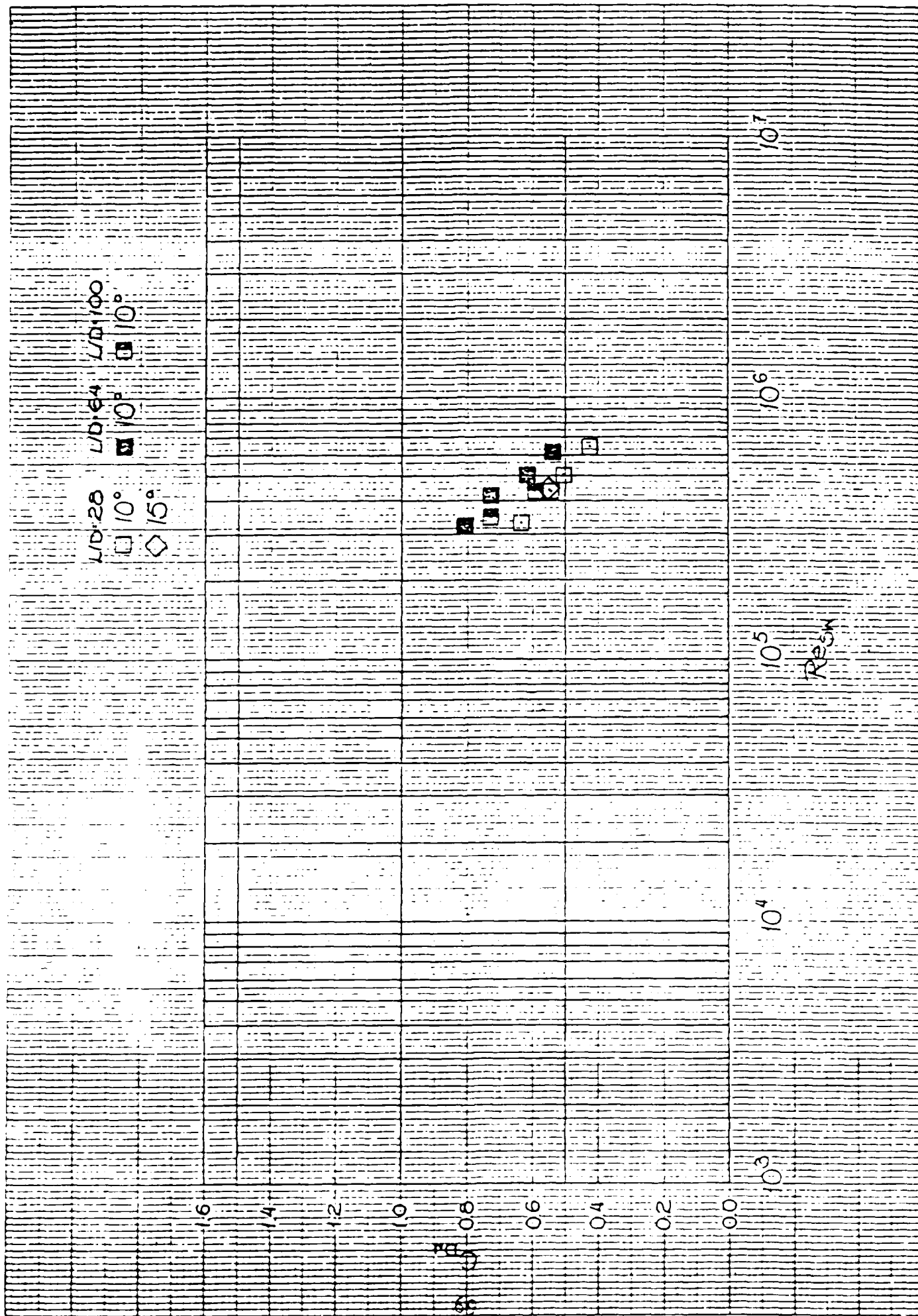


Figure 15. Plot of  $\bar{C}_{pN}$  versus  $Re_{sw}$  for the same supercritical data plotted in Figure 14.

100-5581-100

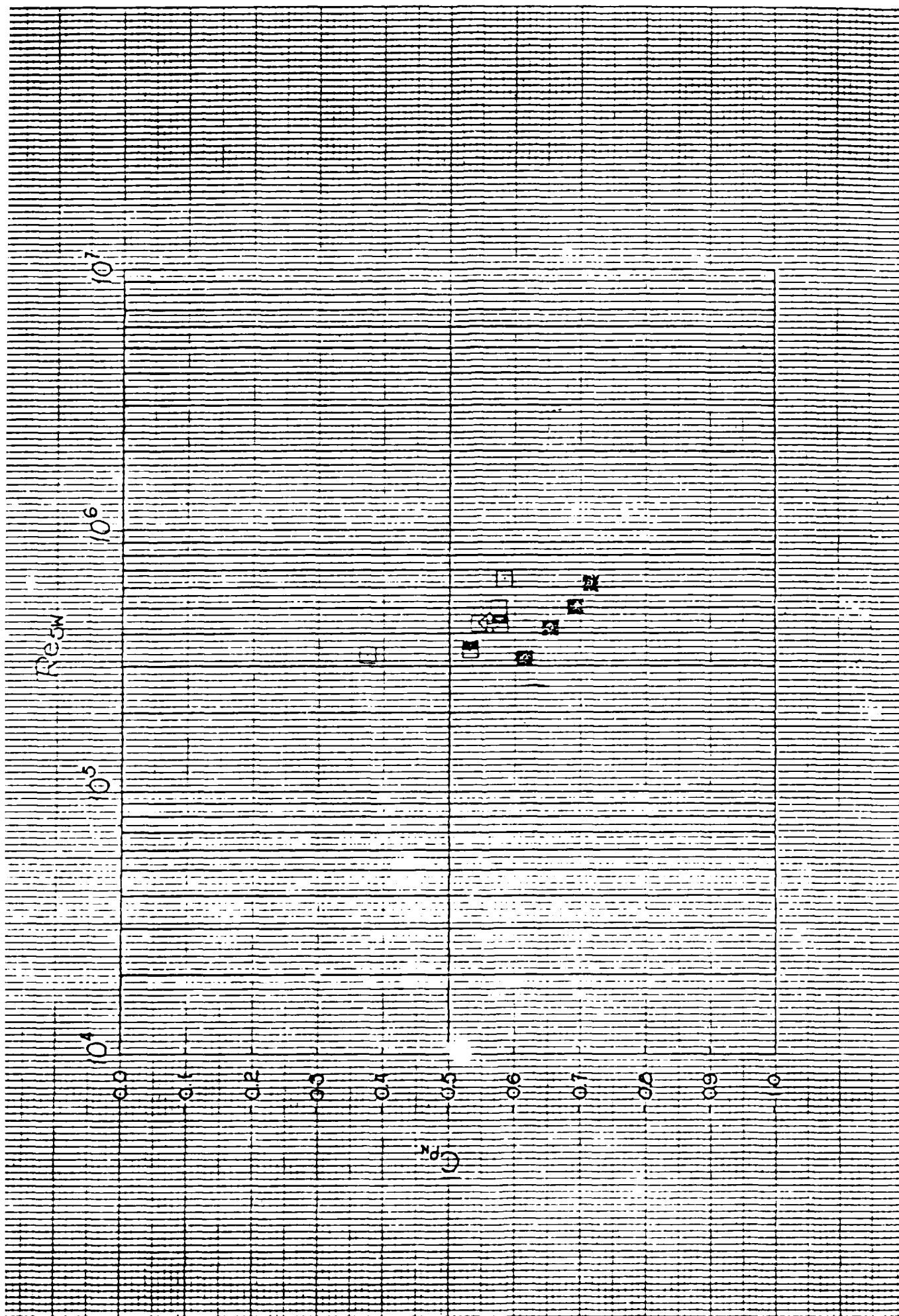


Figure 16. Isolated plot of  $\bar{C}_p$  versus  $\gamma$  for the supercritical data shown in Figures 14 and 15. The symbols  $\square$ ,  $\diamond$ ,  $\triangle$ , and  $\nabla$  represent  $U_\infty = 113, 147, 179, \text{ and } 223$  ft/sec with the open, solid, and two tone points corresponding to L/D ratios of 28, 64, and 100 respectively.

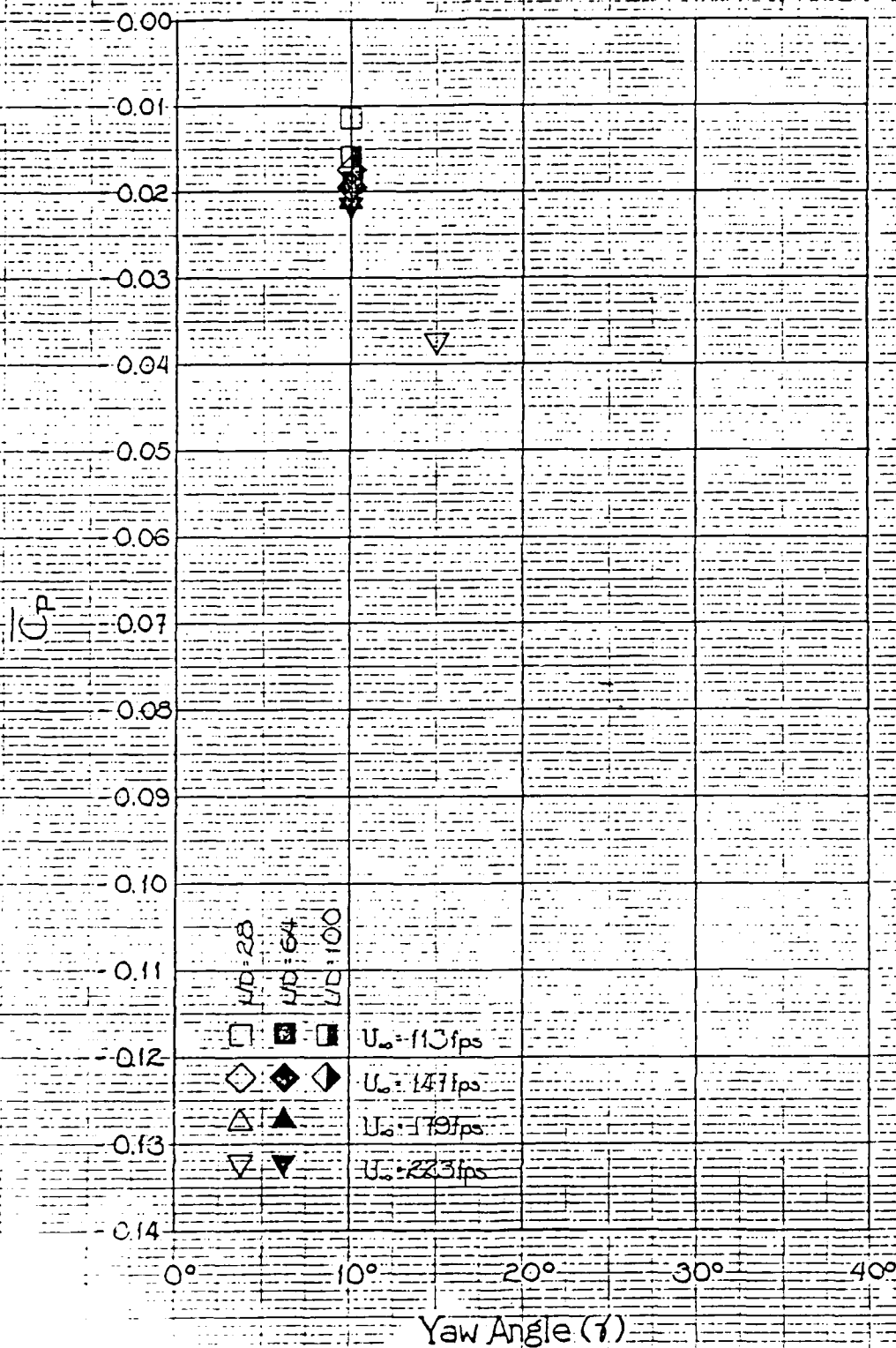


Figure 17. Representative sketches of the three types of  $C_{pN}$  versus  $\theta$  profiles reported thus far; (a) laminar separation, (b) transitional, and (c) turbulent separation. The quantitative information in these plots is approximate.

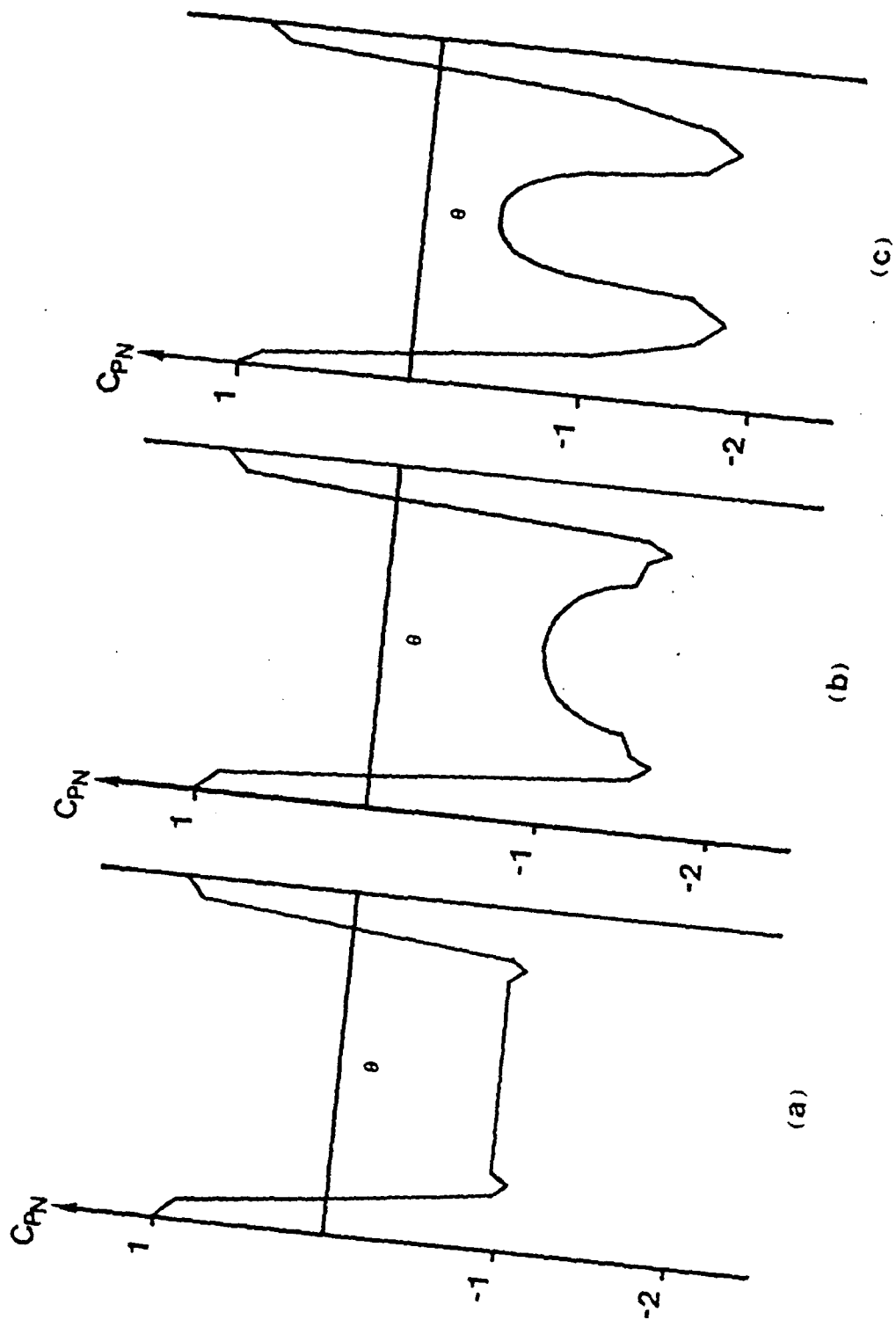


Figure 18. Representative example of an asymmetric type of  $C_{pN}$  versus  $\theta$  profile along with a potential solution profile. The profile was taken for  $U_\infty = 114$  ft/sec,  $\gamma = 17.5^\circ$ , and  $L/D = 64$ .

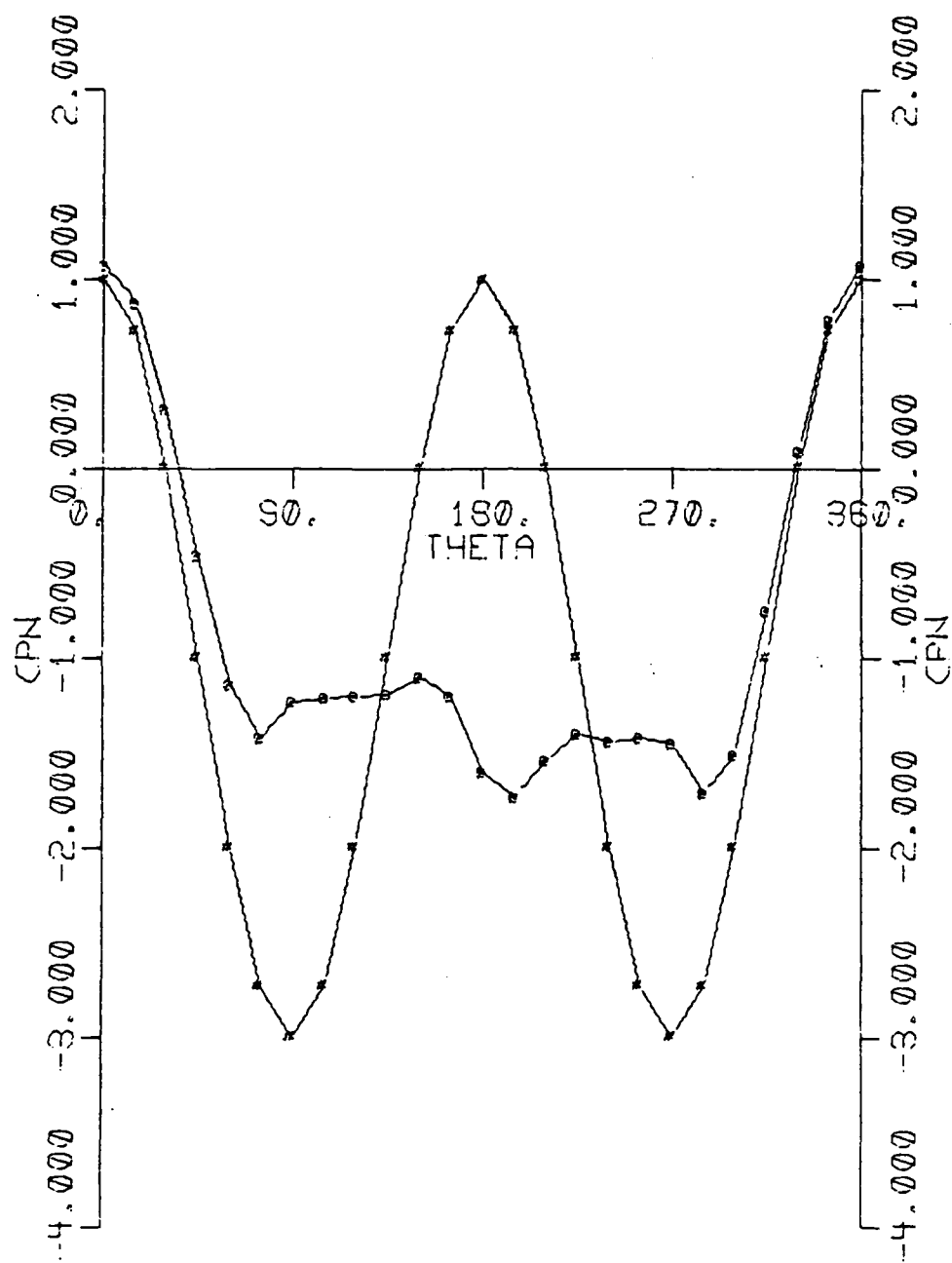


Figure 19. Representative example of an asymmetric type of  $C_{pN}$  versus  $\theta$  profile along with a potential solution profile. This profile was taken at  $U_\infty = 61$  ft/sec,  $\gamma = 15^\circ$ , and  $L/D = 64$ .

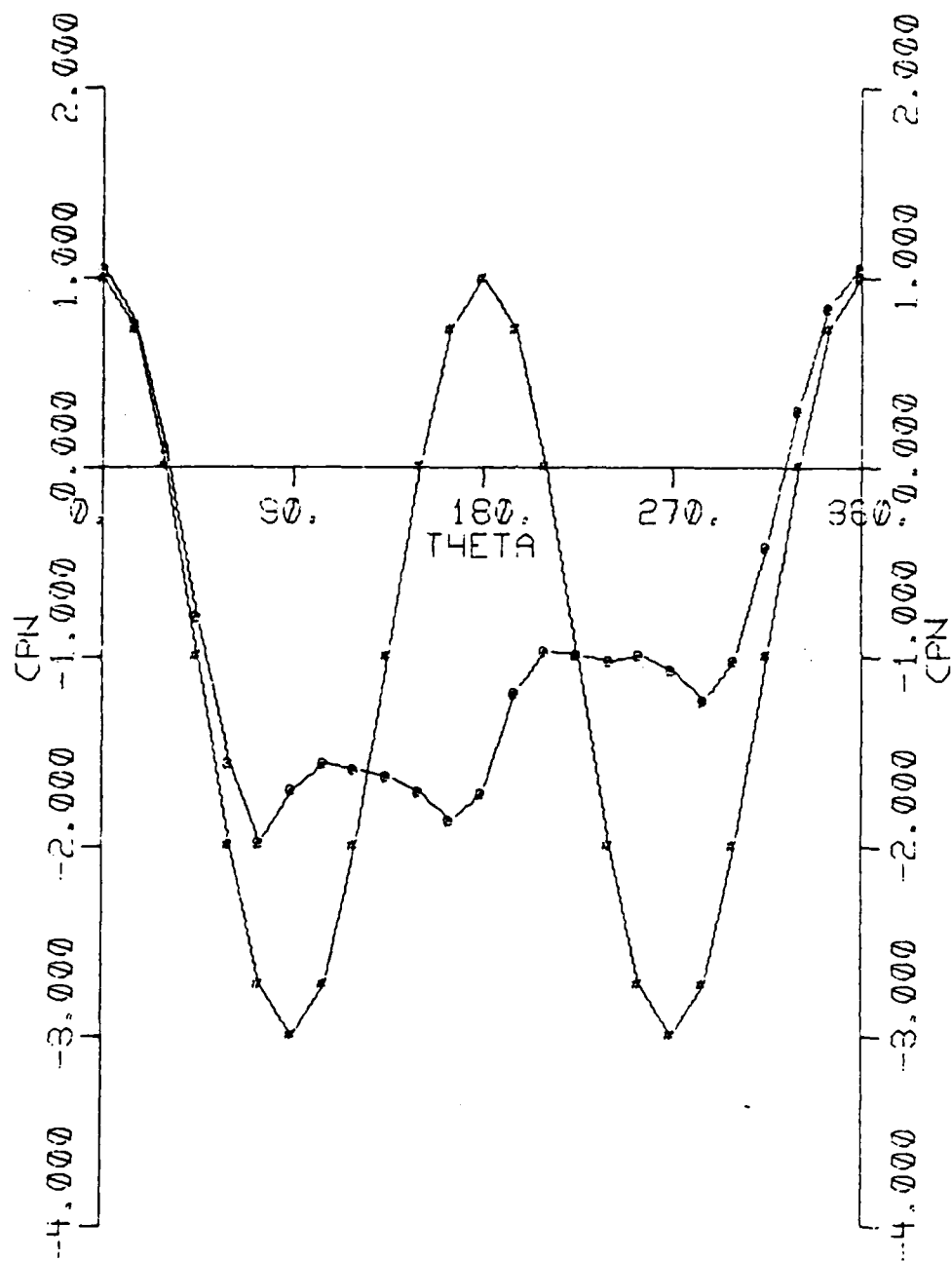


Figure 20. Plot of  $C_{DN}$  versus  $Re_{sw}$  for the asymmetric profile data. The open, solid, and two tone points are representative of the L/D ratios, 28, 64, and 100 respectively. The symbols  $\bigcirc$ ,  $\square$ ,  $\diamond$ , and  $\triangleright$  correspond to yaw angles of  $5^\circ$ ,  $10^\circ$ ,  $15^\circ$ , and  $17.5^\circ$  respectively.

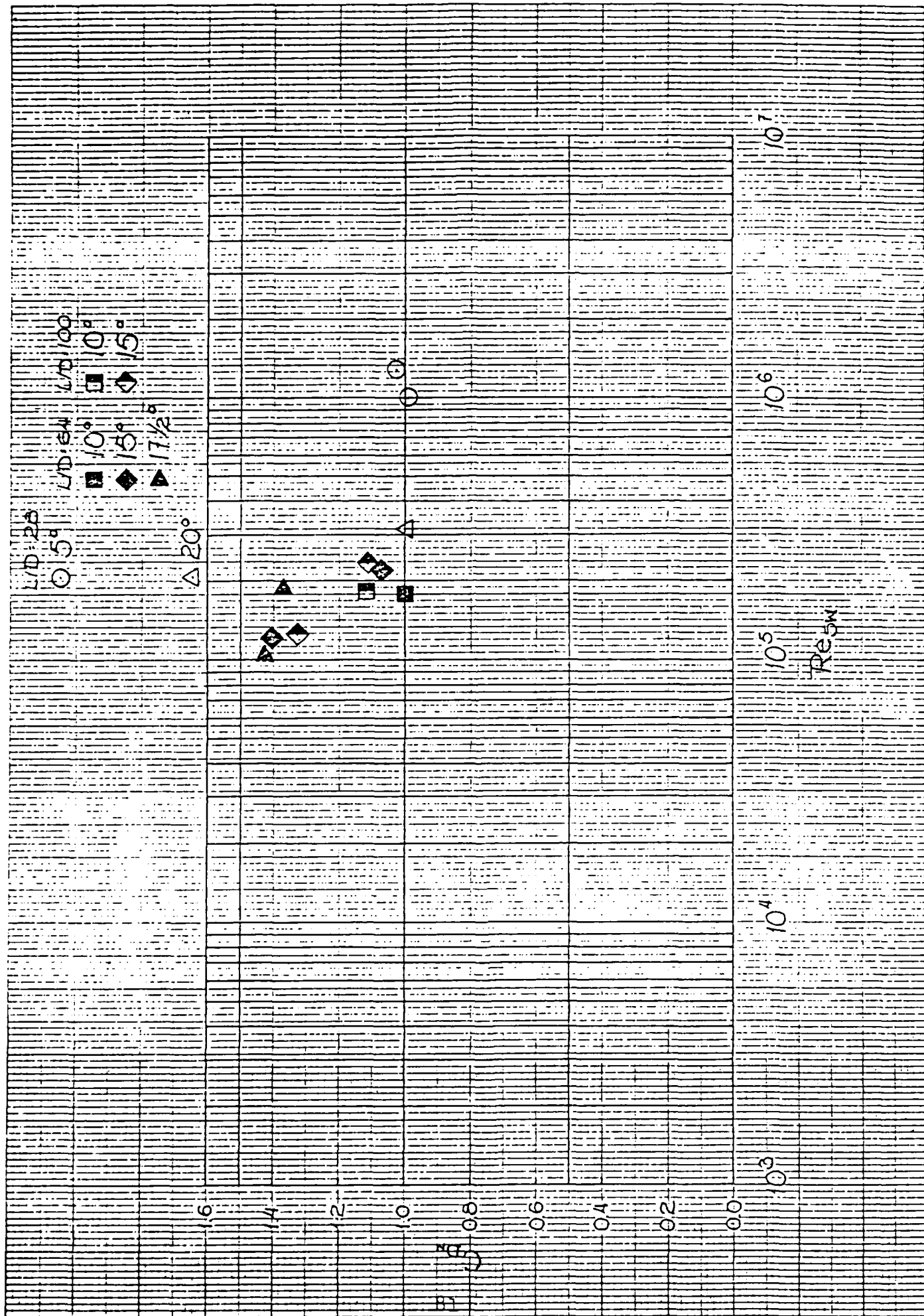


Figure 21. Plot of  $\bar{C}_{pN}$  versus  $Re_{sw}$  for the same asymmetric profile data shown in Figure 20.

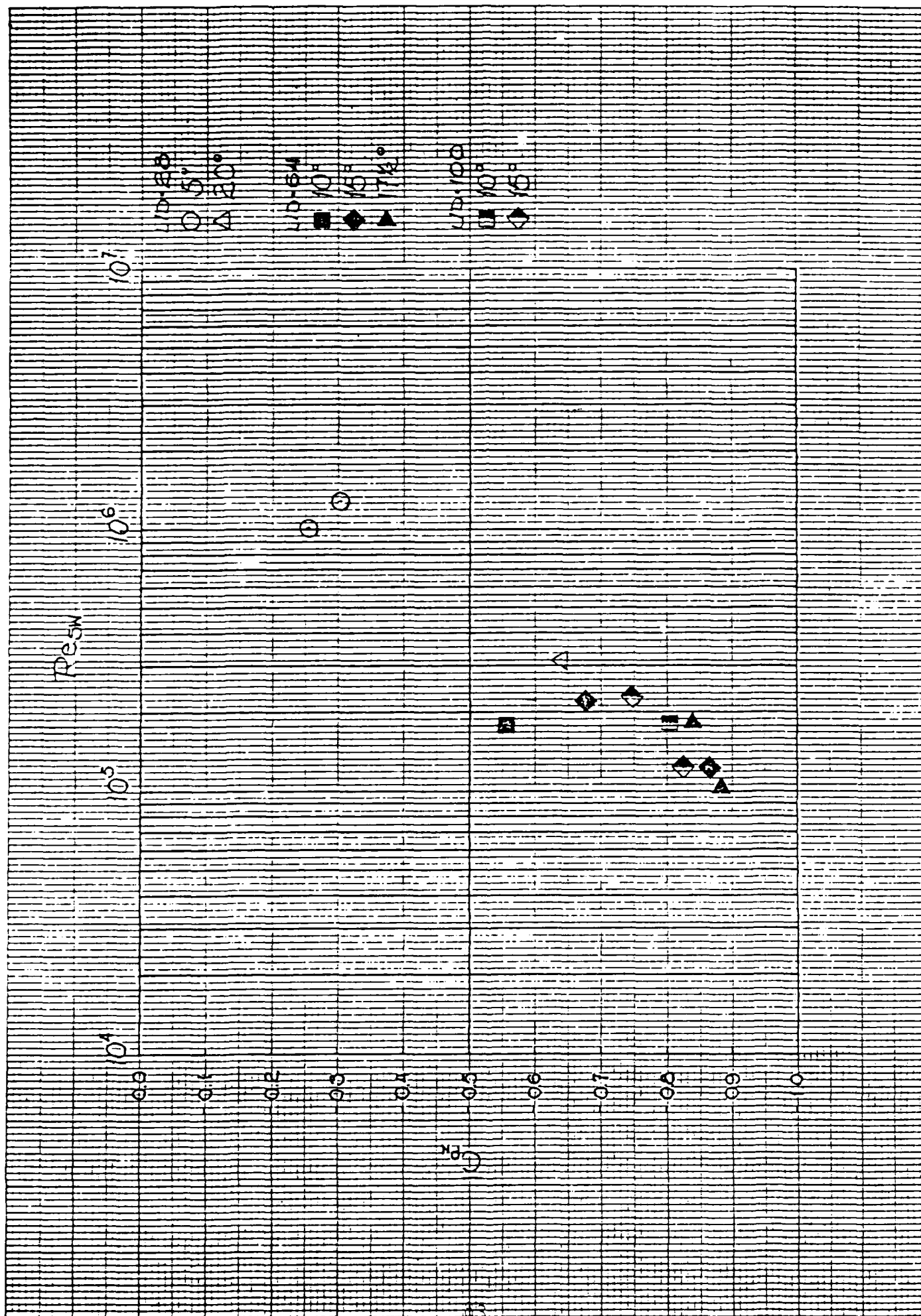


Figure 22. Isolated plot of  $\bar{C}_p$  versus  $\gamma$  for the asymmetric data shown in Figures 20 and 21. The  $\bigcirc$ ,  $\square$ ,  $\triangle$ , and  $\nabla$  shapes correspond to  $U_\infty = 61, 113, 179, \text{ and } 223 \text{ ft/sec}$ . Again, the open, solid, and two tone points represent L/D ratios of 28, 64, and 100 respectively.

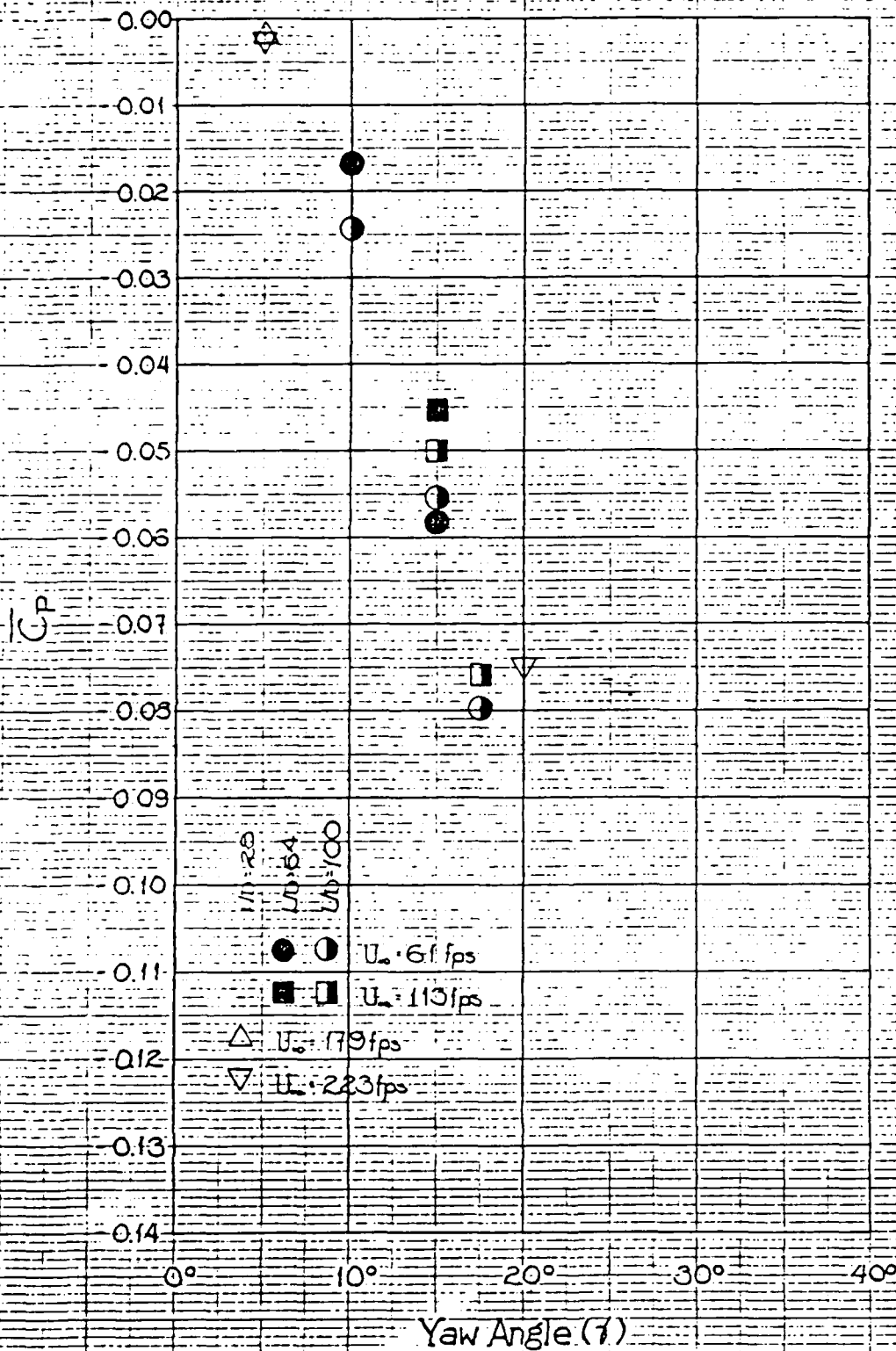


Figure 23. Combined plot of  $C_{DN}$  versus  $Re_{sw}$  comparing the results of the present study with those of Bursnall and Loftin (1961) and solid points correspond to  $Re_{sw}$  of 28 and 64 while Bursnall data appear as two tone air

AD-A102 355

STATIC PRESSURE DISTRIBUTION ON LONG CYLINDERS AS  
FUNCTION OF ANGLE OF VA. (U) MICHIGAN UNIV ANN ARBOR  
DEPT OF AEROSPACE ENGINEERING T WEI ET AL. JUL 83

2/2

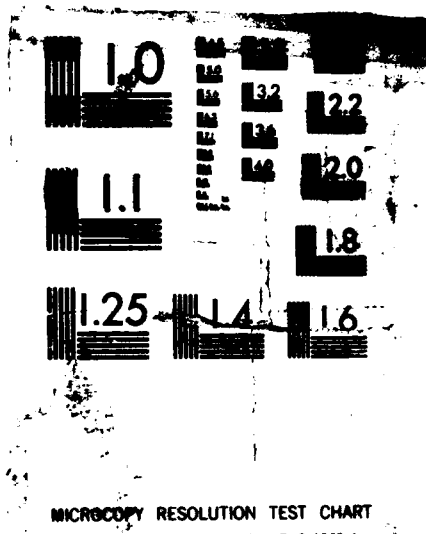
UNCLASSIFIED

N00014-76-C-0571

F/G 20/4

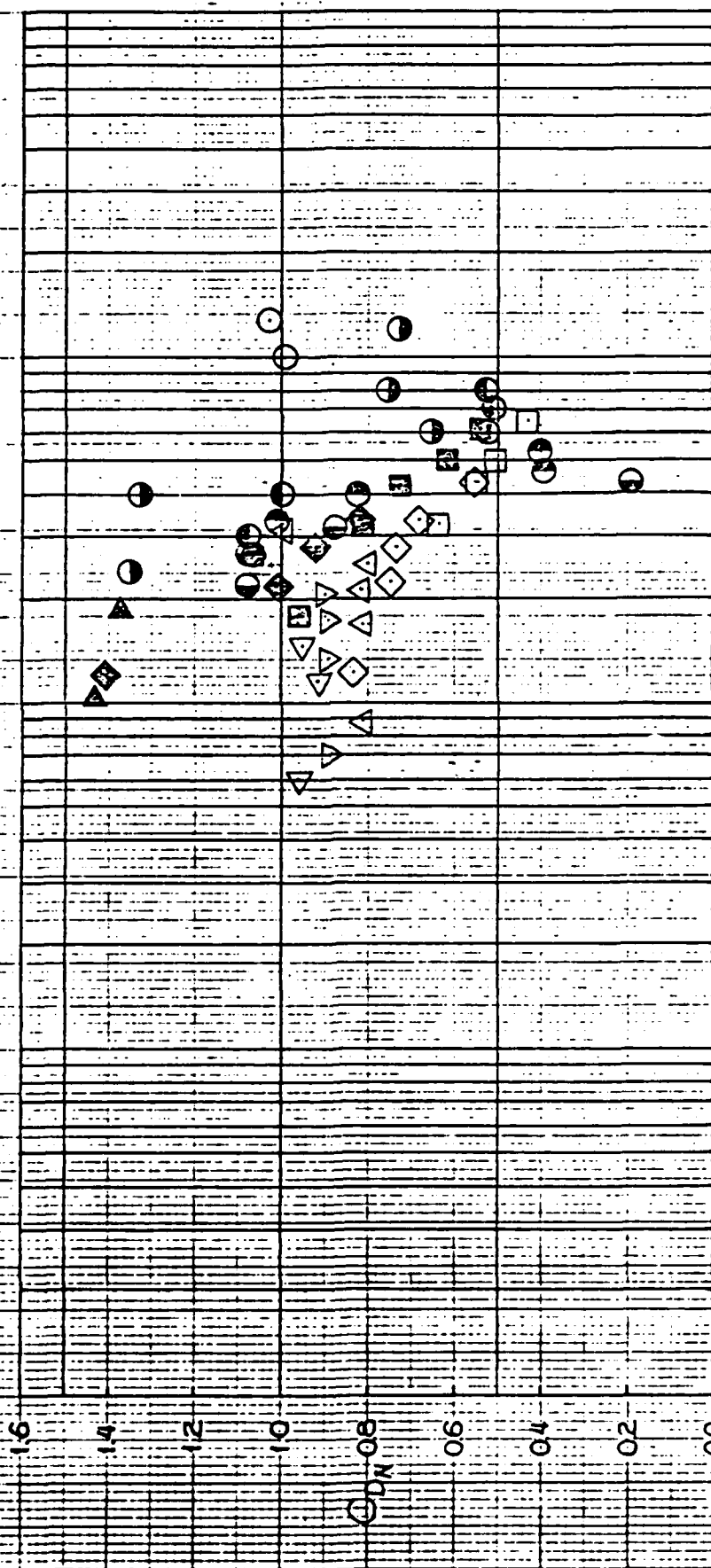
NL





UP 28 64 THRESHOLD LOSS

SYMBOL ○ □ ◇ △ ▽ ◊ ◆ ▲ ● ○ ● ●  
 VALUE 5 10 15 20 25 30 10 15 17 15 60 45 30



10<sup>3</sup> 10<sup>4</sup> 10<sup>5</sup> 10<sup>6</sup> 10<sup>7</sup>  
 Resw

Figure 24. Linear regression fit lines of the data in Figure 23. The solid line is a fit of Bursnall and Loftin's (1951) 60° and 75° angle data. — . — represents the L/D = 28 fitted line, — .. — corresponds to the L/D = 64 fitted line, and the dashed line is a reproduction of the 90° yaw curve plotted in Schlichting (1979).

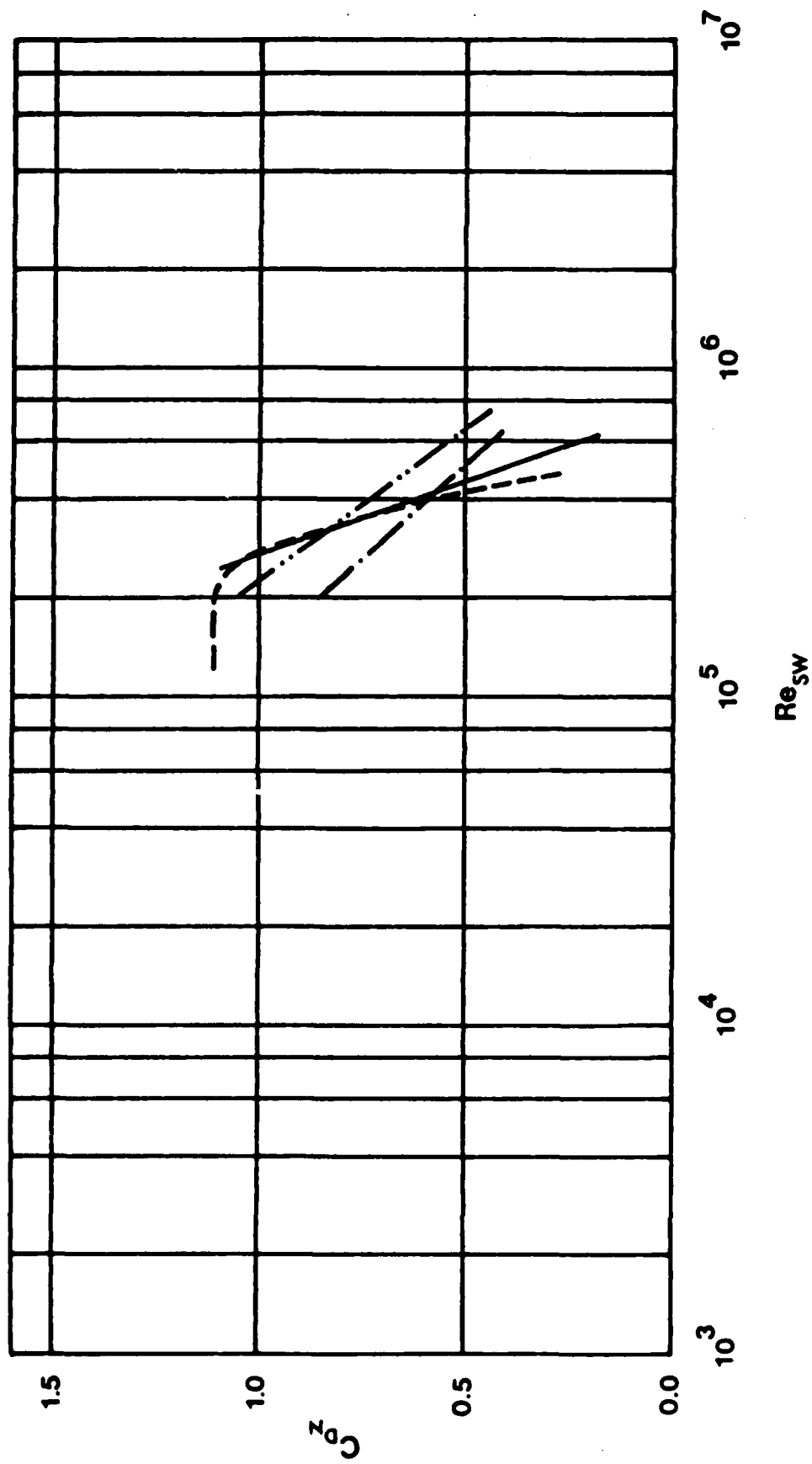


Figure 25. Linear regression fit lines of the data in Figure 23. The solid line is a fit of Bursnall and Loftin's (1951) 30° and 45° angle data. Again — . — represents the  $L/D = 28$  fitted line, and — .. — represents the  $L/D = 64$  fitted line.

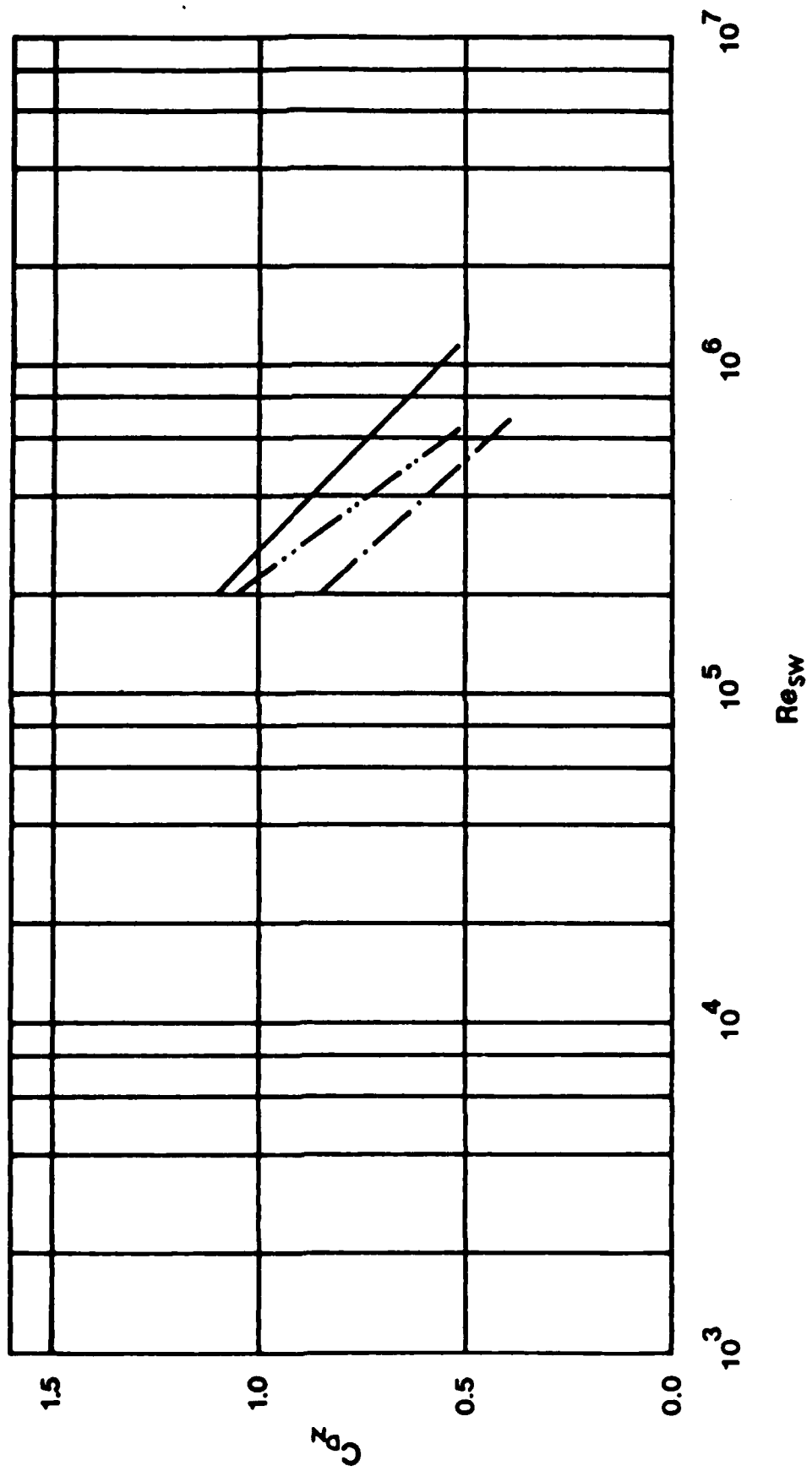


Figure 26. Combined plot of  $\bar{C}_{pN}$  versus  $Re_{sw}$  for the present study. Open, solid, and two tone points correspond to the L/D ratios, 28, 64, and 100 respectively.

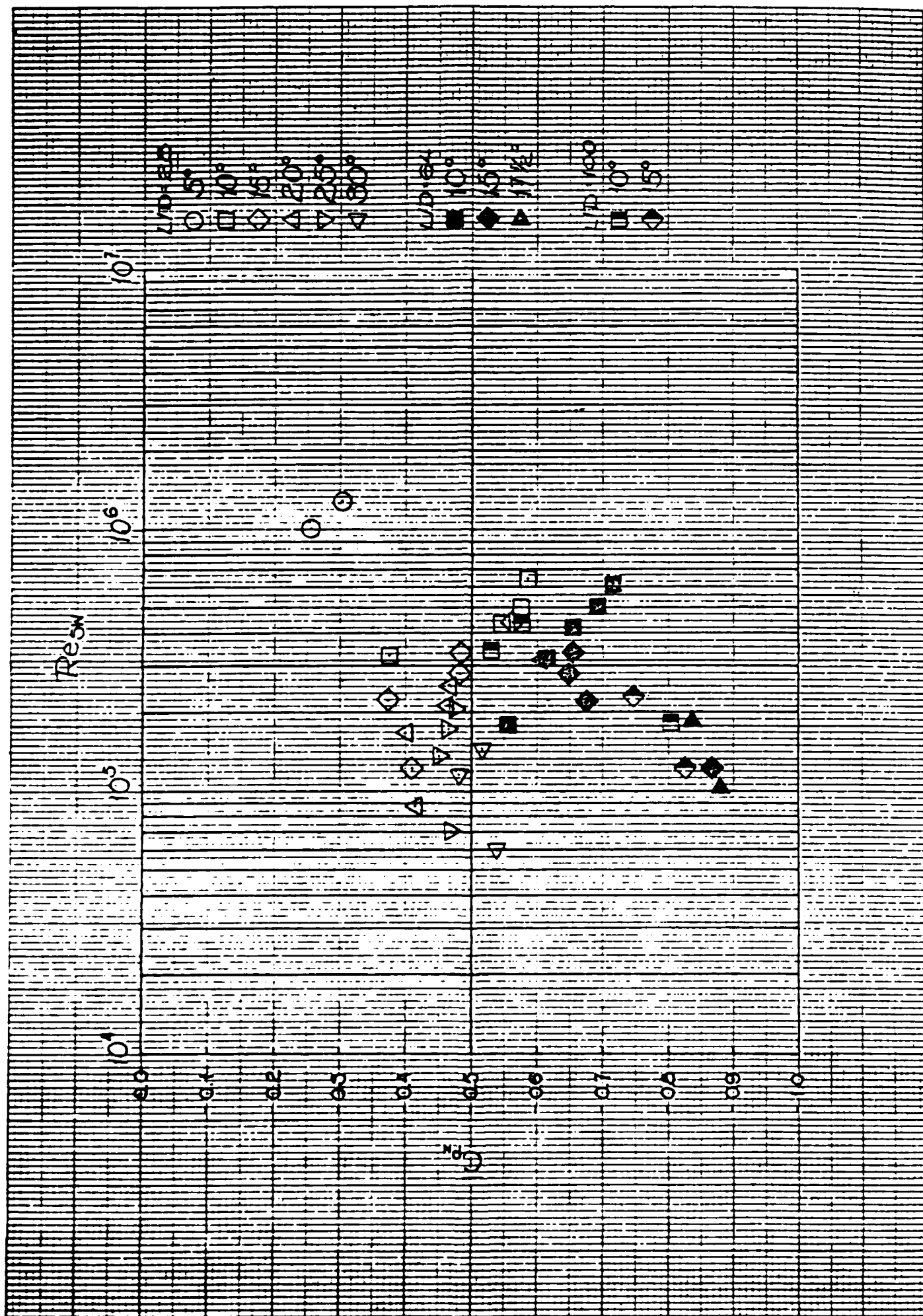


Figure 27. Trend lines of the  $L/D = 28$  data  
(— - —), the  $L/D = 64$  data  
(———), and Roshko's (1961) base  
pressure coefficient data (-----).

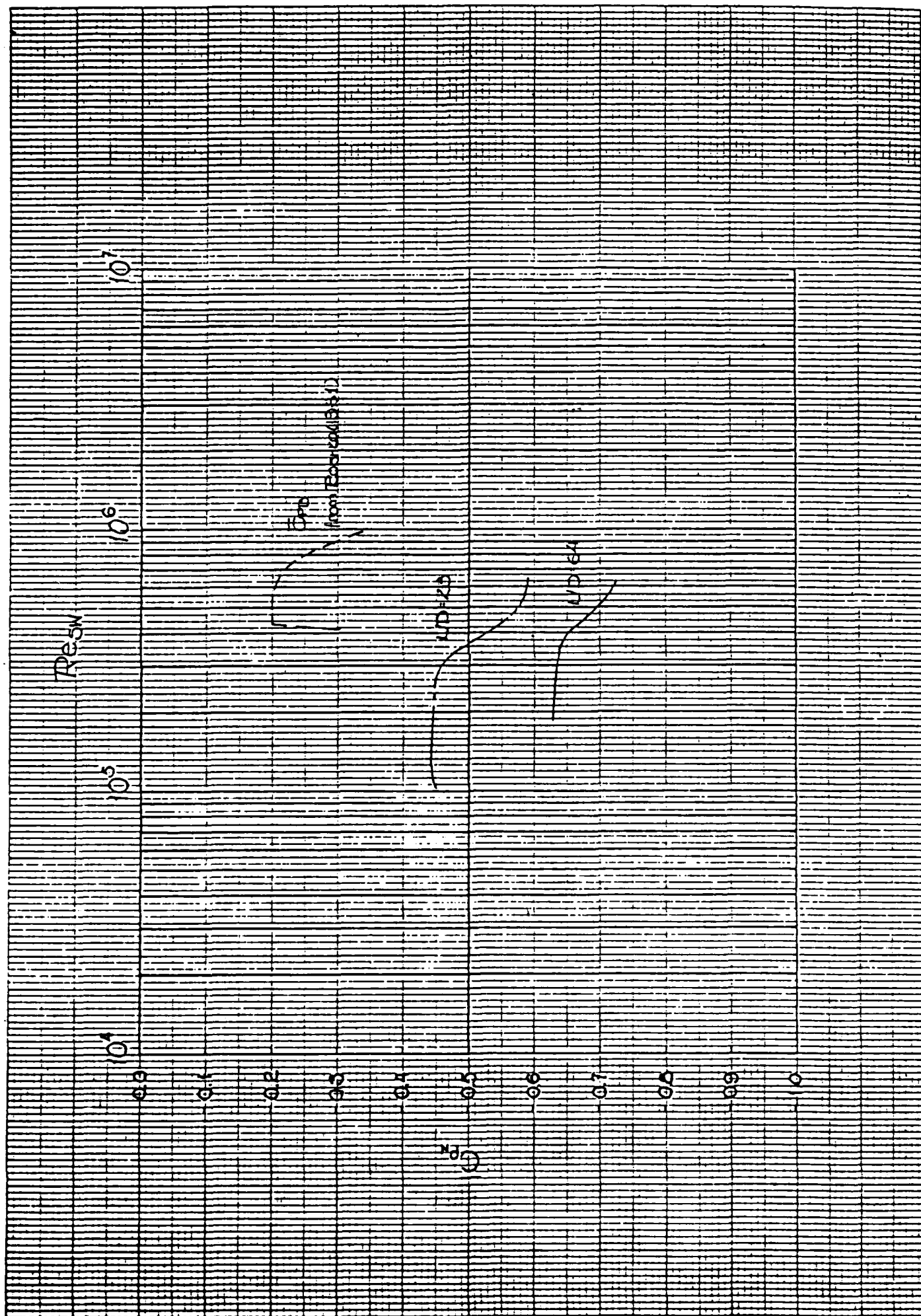


Figure 28. Example of a  $C_{pN}$  versus  $\theta$  profile which does not fall into any of the four categories already reported. The profile was taken at  $U_\infty = 179$  ft/sec,  $\gamma = 5^\circ$ , and  $L/D = 64$ .

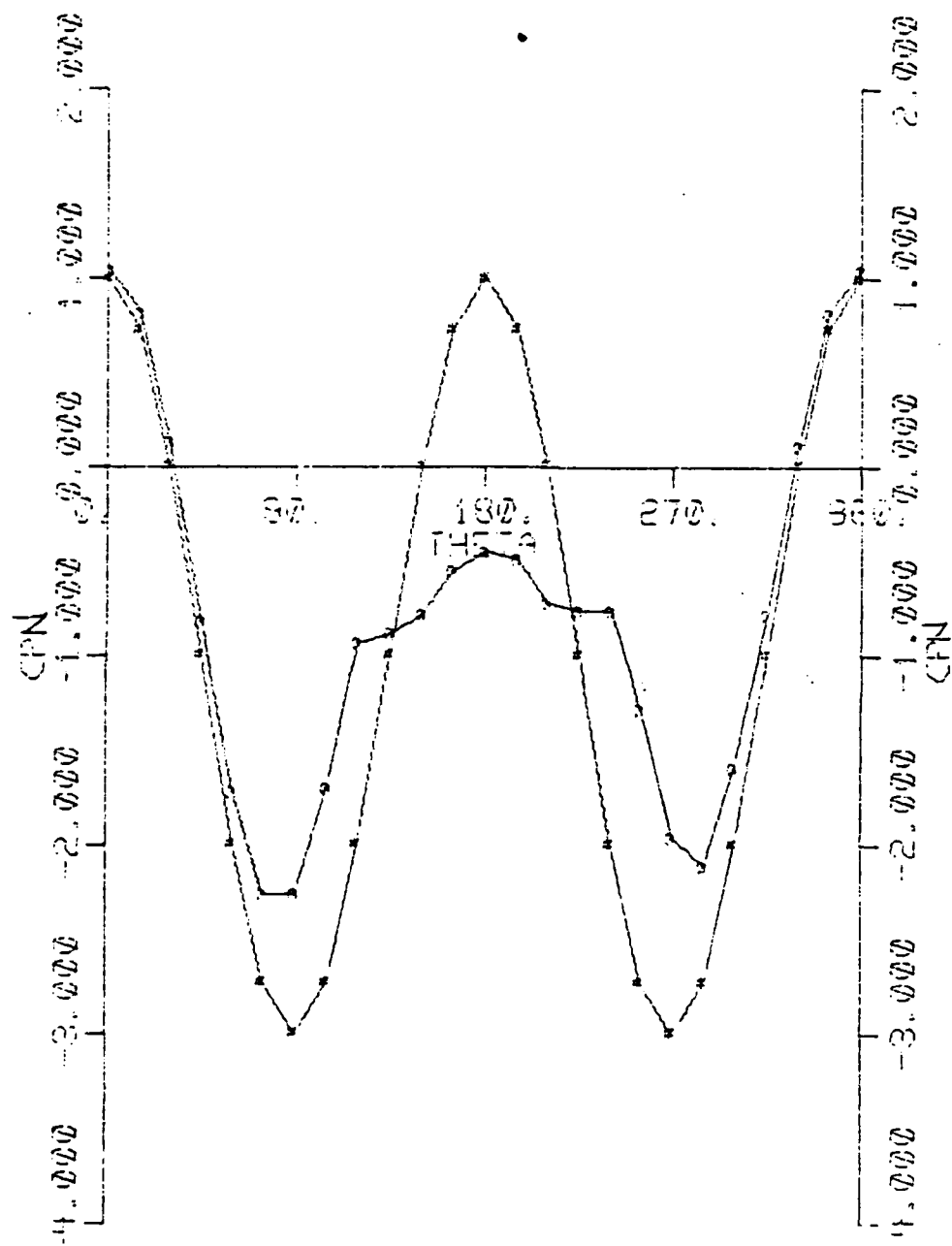


Figure 29.  $C_{DN}$  versus  $Re_{sw}$  plot for the small yaw angle data which did not fall into the subcritical, transitional, supercritical, or asymmetric categories. The symbols  $\circ$ ,  $\square$ ,  $\diamond$ , and  $\triangle$  represent yaw angles of  $1^\circ$ ,  $2^\circ$ ,  $2.5^\circ$ , and  $5^\circ$  respectively. The open, solid, and two tone points correspond to the L/D ratios of 28, 64, and 100.

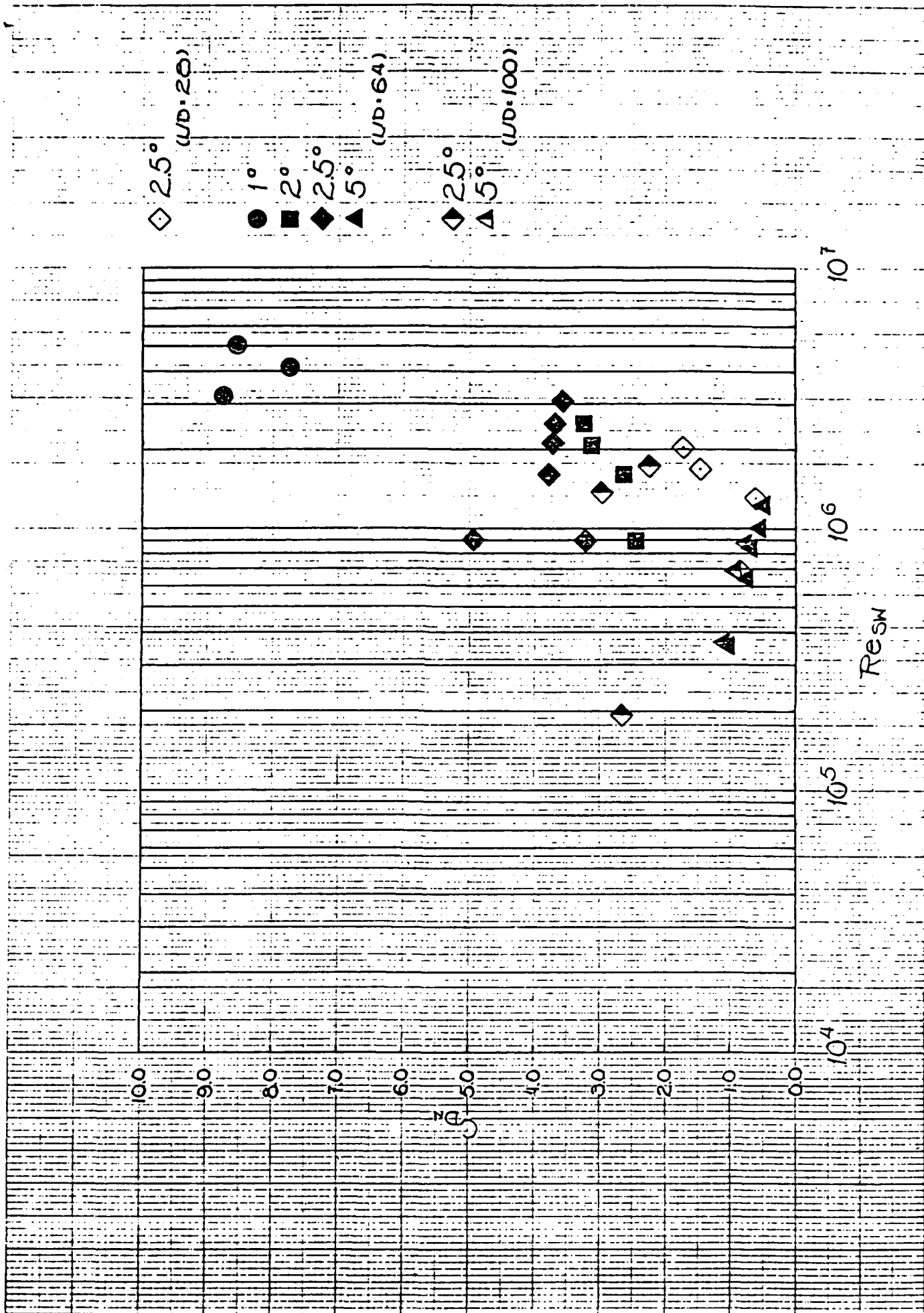
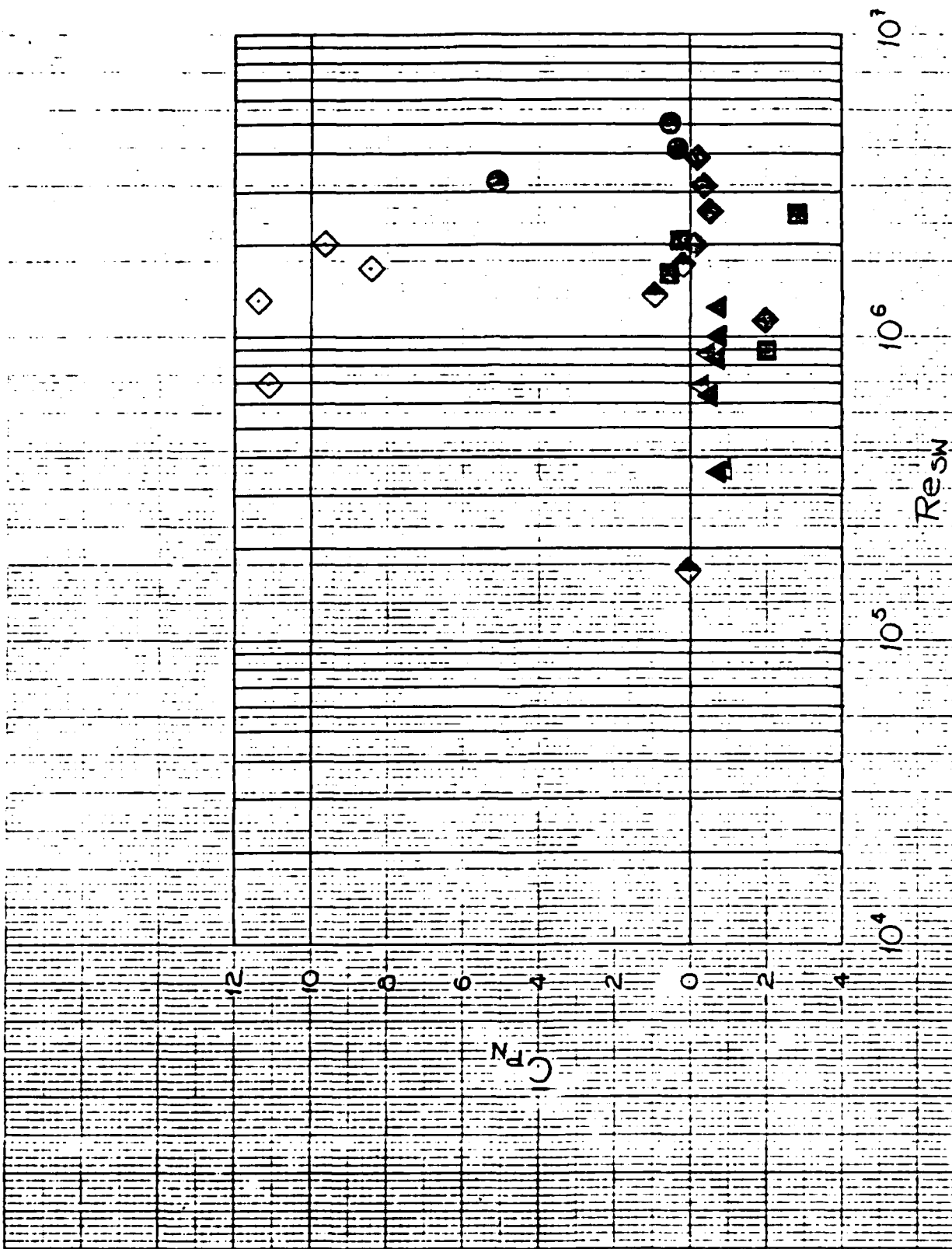


Figure 30.  $\bar{C}_{pN}$  versus  $Re_{sw}$  plot for the same small angle data shown in Figure 29.



END

8-87

DTIC